Article

A Geometry-First Design Framework and Interactive Design Tool for 3D-Printed Microfluidic Valves Using New Photopolymer Resins

Huu Anh Minh Nguyen [1], Quynh Ai Vuong [1], Nhu Doan Quynh Nguyen[1], Dae Jung Martins Cruz [3], Bernardino Almanzar [3], Aidan Kinney [1], Abigail Goz [5], Maanit Khanna [1], Rishabh Jitender [1], Sergei Chapek[4], Mark Volosov[3] and Roman Voronov [1,2,3*]

[1] Otto H. York Department of Chemical and Materials Engineering, Newark College of Engineering, New Jersey Institute of Technology, University Heights, Newark, NJ 07102, USA.
[2] Department of Biomedical Engineering, Newark College of Engineering, New Jersey Institute of Technology, University Heights, Newark, NJ 07102, USA.
[3] AltVIVO, Inc., Newark, NJ 07105, USA
[4] Independent Researcher, Rostov-on-Don, Russia.
[5] Department of Computer Science, Ying Wu College of Computing, New Jersey Institute of Technology, University Heights, Newark, NJ 07102, USA.
* Corresponding author: Prof. Roman Voronov.Email: rvoronov@njit.edu

Abstract

Microfluidic valves are essential for routing, isolation, and automation in integrated microfluidic systems, yet they remain difficult to fabricate in 3D-printed workflows: a functional valve requires a thin, pressure-responsive membrane within an otherwise rigid monolithic print — a combination that vendor datasheets do not predict. With no consensus material for 3D-printed microfluidics and new resins appearing continually, valve development in practice devolves into blind trial-and-error across an inflated space of printer settings and free geometric parameters. Here, we present a systematic, geometry-first framework that establishes valve feasibility for newly adopted photopolymer resins without mechanical property data or iterative guesswork. Using the commercial resin FunToDo NanoClear, we map enclosed-channel printability bounds, identify membrane thickness–width limits, quantify membrane reach with an automated image-analysis pipeline, and prescribe the sealing geometry through an interactive design tool. A single measured constant — the membrane deflection coefficient κ — links these steps, and the closure model underlying the tool is purely geometric and therefore independent of fabrication route. Functional testing validates the framework: tool-prescribed valve seats decouple sealing from channel width, and the optimized valves block flow completely, tolerate control pressures up to 60 psi, and sustain one million open/close actuation cycles at all but the widest tested channel width — matching the highest lifetime reported for a 3D-printed membrane valve, previously achieved only with a custom thermally post-cured resin, here obtained with an off-the-shelf commercial material. The framework also generated a previously unreported squeeze-valve redesign in which two mirrored spherical-cap seats, prescribed by the same κ, guide opposed floor and ceiling membranes to closure. Its generality was reaffirmed by producing valves from Asiga Dental IBT, a dental resin never before used for microfluidics, and the valves were integrated into device-level demonstrations including multi-way flow routing and an on-chip pump.

1. Introduction

Microfluidic valves are essential for routing, switching, metering, and isolating flows in integrated microfluidic networks, and are therefore key enablers of automation and high-throughput operation. Traditionally, such valves have been fabricated by multilayer soft-lithography and related assembly-based workflows, which can produce sophisticated devices but typically yield predominantly planar or layered architectures and often require repeated alignment, bonding, and other labor-intensive manual steps. Light-based additive manufacturing methods, particularly digital light processing (DLP) and stereolithography (SLA), are attractive alternatives because they build enclosed three-dimensional structures monolithically, thereby reducing the need for manual bonding while also offering high spatial resolution relative to many other rapid-prototyping alternatives used in microfluidics[1-3]. In these methods, a liquid photopolymer is selectively crosslinked in a layer-by-layer manner to form the desired structure[2, 4, 5], making them well suited in principle for integrated devices containing many embedded channels and valves distributed across different heights and orientations[5-7]. For membrane-based valves, this resolution is especially important not only for defining small channels, but also for forming a thin suspended membrane with controlled thickness, width, and functionality. At the same time, the fabrication of functional valves remains substantially more demanding than the fabrication of simple printed channels, and light-based printing carries well-known photopolymer-specific challenges that must be managed through material choice and post-processing. In particular, vat-photopolymerized parts are seldom fully crosslinked as printed, so residual monomer, unreacted photo initiator, and unbound oligomers can leach from channel walls unless sufficiently removed during washing and post-curing—a recognized concern when the channels subsequently contact live cells, biological samples, or sensitive reagents [8, 9].

For membrane valves in particular, the fabrication-specific challenges are more severe. A monolithic printed microfluidic valve must simultaneously satisfy two difficult requirements. First, the printing process must preserve small enclosed negative spaces and allow uncured resin to be removed from them after fabrication. Second, it must create a membrane thin and compliant enough to deflect under pneumatic control pressure into an underlying flow channel, while the surrounding device body remains rigid enough to support the channel network and sealing interface. In other words, the same print must successfully realize both an enclosed flow architecture and a pressure-responsive membrane within a rigid monolithic structure. Even for simple membrane-valve geometries, feasibility depends on a strongly coupled set of parameters spanning both the flow side and the control side, including channel width and height, membrane thickness, chamber width and curvature, and auxiliary sealing features[5, 6, 10-18]. Because these variables interact strongly, the first major challenge is often not valve optimization, but identifying what can be printed reproducibly at all.

Furthermore, despite the promise of light-based printing, 3D-printed microfluidics still lacks a standard valve material[2, 19-21]. In conventional soft-lithography workflows, PDMS serves as a de facto elastomeric baseline in academic research, with well-characterized valve behavior despite important limitations that constrain broader commercial use[22-28]. By contrast, light-based microfluidic printing draws from a broad and expanding set of material options, including custom resin formulations[1, 19, 20], and repurposed photopolymers such as dental materials[29], each with distinct optical and mechanical properties[1, 10, 19, 20].

This lack of standardization is evident in prior successful demonstrations of 3D-printed membrane valves from leading groups, which have relied on custom PEGDA-based formulations rather than off-the-shelf commercial resins, and have also varied in printer platform, valve archetype channel profile, and use of auxiliary sealing features[5, 6, [10-18]. These studies established important proof-of-concept advances, but they also show that successful valve designs are often tightly coupled to a particular resin-printer-post-processing combination. As a result, reproducing the literature may require custom chemistry, tuned exposure conditions, specialized post-curing procedures, or geometry tailored to a specific material system. Thus, navigating this multidimensional design space creates a steep learning curve with too many coupled variables for a newcomer to explore efficiently. Furthermore, the difficulty is compounded by the fact that vendor documentation often omits the cured mechanical information most relevant to membrane feasibility, leaving users to evaluate unfamiliar materials with incomplete guidance; moreover, bulk mechanical measurements may not translate to microscale membrane behavior.

Therefore, these challenges motivate a simpler and more reproducible starting point for valve development. Rather than varying material, process, and geometry simultaneously, we propose a geometry-first framework that uses commercially available printers, commercially available resins, and default manufacturer-validated print settings (by fixing all printer settings and excluding them from the study, the problem is reduced to a geometry-only design space, allowing the effect of geometry on printability to be isolated). The framework proceeds as follows: first, it maps printability bounds to determine what is printable and what isn't (see Section 3.1); then, it evaluates membrane function within the printable region (see Section 3.2); and, lastly, it derives the required sealing geometry from a single experimentally measured membrane-deflection constant through a geometric closure model (see Section 3.3.3), which we package as an interactive design tool (provided in the ESI). One conservative starting point within this approach is to examine a stringent closure case requiring broad membrane deflection over a rectangular flow channel; when that demand proves excessive, conditional geometric modifications such as raised doormats or alternative channel profiles can be introduced to localize sealing and reduce the required closure distance[6, 12-18]. The trade-off for fixing process settings is that this strategy may sacrifice some achievable resolution and may not immediately yield the smallest possible valve dimensions. We nevertheless consider that trade-off worthwhile because it provides a practical, lower-barrier entry path by which a user can begin valve development without first mastering custom resin formulation or extensive process optimization. In that sense, the framework is intended both to replace guesswork with a logical entry strategy for membrane-valve design in unfamiliar photopolymers and to provide a systematic way to adapt literature-derived valve geometries when direct transfer to a new resin is unsuccessful. Moreover, the framework is not limited to commercial materials: it applies equally to custom-formulated resins, where it can guide and accelerate valve design in the same way.

In this work, we implement that framework on the Asiga platform, which is widely used in light-based microfluidic printing and supports a large open library of more than 650 resins with predefined machine settings[30]. This open-material, vat-photopolymerization (DLP/SLA) setup is the fabrication modality our framework targets—chosen for its accessibility in producing monolithic enclosed channels and membranes—rather than mask-based photolithography (e.g., SU-8) or two-photon direct-write (e.g., Nanoscribe IP-L), which address different fabrication regimes. We first develop the framework using FunToDo NanoClear as an intentionally challenging case: although NanoClear is a commercially available optically clear resin already used in microfluidic fabrication[31-36], there are, to our knowledge, no prior reports of printed microfluidic valves in this material; and, its suitability for membrane-based valve operation is not obvious from the available material information[37]. We then test the framework on a second and more challenging commercial resin, Asiga Dental IBT, a dental material that, to our knowledge, has not previously been used for microfluidic fabrication at all, in order to determine whether the same geometry-first logic remains useful beyond a single favorable formulation[38]. Along the way, we fabricate all three canonical membrane-valve archetypes (Quake, Plunger, and Squeeze) monolithically, and report a novel Squeeze-valve redesign inspired by the geometric framework developed herein. In this way, the manuscript asks not whether published valve geometries can be copied unchanged, but how they can be translated into new commercial-resin systems under fixed default process settings, even if some minimum achievable valve size is sacrificed in the process. Together, these case studies show that membrane-valve development can be approached systematically using commercial materials and default print settings, while preserving a path toward later refinement if a user chooses to optimize resin or process conditions to reduce the valve size.

2. Materials and Methods

2.1. Resins

NanoClear (FunToDo / Ergometa distribution) was used as the demonstration resin in this study. NanoClear is marketed as a high-resolution, optically clear photopolymer suitable for fine-feature fabrication. Since no manufacturer-provided technical datasheet reporting mechanical properties relevant to membrane deformation or overhang stability is available, the only publicly accessible specifications are those listed on the vendor's website.[37] These specifications include basic physical and processing parameters but do not provide the elastic, flexural, or failure properties required to predict membrane-based valve feasibility: viscosity (83 mPa·s at 25 °C), density (1.02 g cm^{-3}), shrinkage (<0.2%), recommended Z-axis layer height range (2–200 μm), storage conditions, and washing guidelines. The website also reports a single mechanical property, hardness (Shore D 85). No additional mechanical properties—such as modulus, tensile strength, or elongation—are published.

Asiga Dental IBT (Asiga, Australia) was used as a secondary demonstration material to evaluate the generality of the proposed geometry-first framework across chemically and mechanically distinct photopolymers. Dental IBT is a commercially available, optically clear photopolymer formulated for orthodontic indirect bonding trays and is not marketed for microfluidic device fabrication. Publicly available documentation for IBT includes a Safety Data Sheet (SDS) and an Instructions for Use (IFU) [38], which report regulatory, compositional, and processing information relevant to dental workflows. Reported properties include a dynamic viscosity of approximately 400 mPa·s (liquid state), a flash point exceeding 150 °C, insolubility in water with solubility in common organic solvents, and optical curing optimized for 385 nm illumination. However, these documents do not provide cured mechanical properties relevant to membrane-based microfluidic valve design, including elastic or flexural modulus, elongation at break, or fatigue behavior under cyclic deformation. Consequently, despite being more extensively documented than NanoClear, IBT similarly lacks the mechanical data required to predict membrane feasibility a priori.

Both resins were used exactly as supplied by the manufacturers, without additives, modifiers, or formulation changes, in order to demonstrate a protocol that does not require resin reformulation or specialized chemistry expertise.

2.2. Valve Archetypes and Sealing Features

Three membrane-based valve archetypes, spanning the canonical modes of membrane-channel interaction in microfluidics, were selected for monolithic fabrication in this work (see Section 3.5.1). In the Quake-style valves fabricated here, a flexible membrane deflects downward into the flow channel under applied control pressure and occludes it by direct membrane-floor contact, so that sealing is governed primarily by membrane reach and conformity to the channel floor [6, 11, 12, 18, 39-46]. In the Plunger (membrane-plunger) valves, an intermediate actuation chamber concentrates membrane deformation into a localized, piston-like element that presses into the flow channel — a configuration suited to wider or taller channels [5, 10, 47-53]. In the Squeeze valves, the flow channel is closed from top and bottom simultaneously: opposed floor and ceiling membranes are deflected toward each other by control chambers positioned above and below, pinching the lumen shut across its full height rather than relying on a single membrane occluding against a rigid floor[10, 53, 54].

In all three architectures, auxiliary sealing features — raised valve seats ("doormats") or contoured seat profiles — were incorporated where indicated in Section 3.3 to reduce the required membrane deflection and increase contact pressure at the sealing interface. Because fabrication and operation within a single monolithic print depend sensitively on the coupled geometry of the membrane, flow channel, control chamber, and sealing features, these archetype-specific requirements defined the parameter ranges of the test geometries described next[6, 12, 13, 17, 41, 55, 56].

2.3. Parametric Generation of Test Geometries

All test structures were generated using OpenSCAD version 2021.01, a script-based parametric CAD environment. Two distinct device geometries were used across the framework stages, both designed as cross-sectional mimics capable of providing internal optical access to the valve membrane region (see Figure 1). For the rigid-channel printability sweep (Stage I in Section 3.1), arrays of enclosed channels were fabricated using a parametric geometry in which a thin suspended roof spans a rectangular negative-space channel between two solid sidewalls, open on the front and back faces — hereafter referred to as "Printability Device" (shown in Figure 1A). Throughout this paper, "roof" denotes this printed spanning slab in its passive, structural role, while "membrane" denotes the same physical element in its compliant, functional role once actuated; the two terms therefore describe one feature viewed at different stages of the framework. For the membrane functionality testing (Stage II in Section 3.2), the same channel geometry is extended by adding a sealed pneumatic control chamber directly above the roof, which thereby becomes the actuatable membrane separating the control chamber from the flow channel below — hereafter referred to as "Functionality Device" (shown in Figure 1B). The control chamber must remain enclosed on all sides in order to hold pressure, and its walls clamp the membrane perimeter from above. The flow channel below is open at both its front and back faces: the front face serves as an observation window, while the open back face permits the same transmitted-light (back-illuminated) imaging used for the Printability Devices. The two device types therefore differ only in the presence of the control chamber: in both, the flow-channel roof is carried by the two channel sidewalls with free front and back edges, while in the Functionality Device the membrane perimeter is additionally clamped from above by the control-chamber walls. This difference in support conditions is relevant to the measurements and metrics defined in Section 2.7 and subsequently reported in Sections 3.1 - 3.2. Unless otherwise noted, all devices characterized in Sections 3.1 – 3.4 realize the Quake-style architecture, in which a suspended membrane deflects downward into the flow channel beneath it: the Printability Device isolates the passive roof of that geometry, and the Functionality Device adds the control chamber that actuates it. The Plunger and Squeeze architectures are introduced in Section 3.5.1.

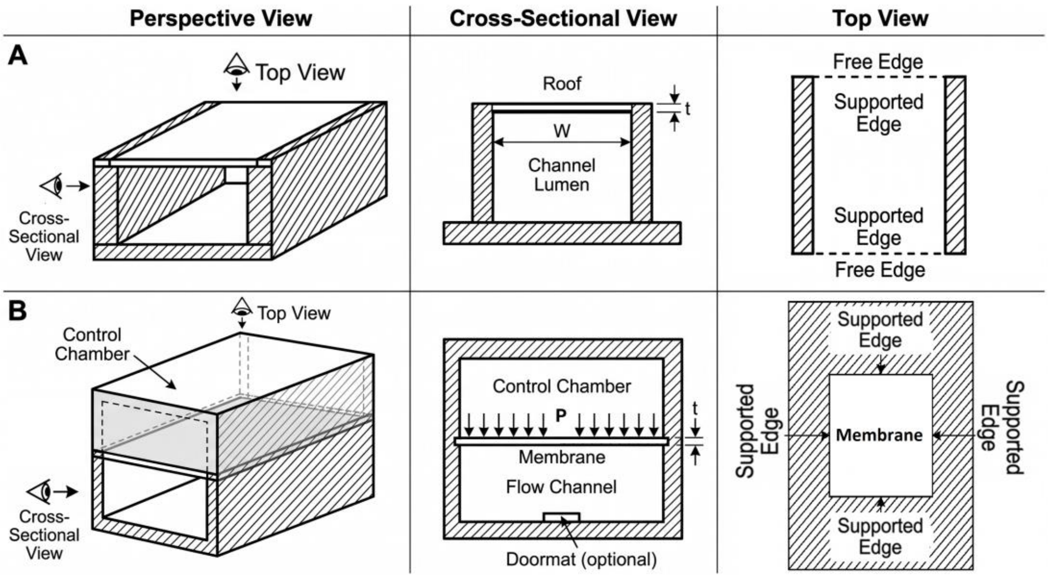

Figure 1 Schematic illustration of the two device geometries used across the framework stages. *(A) "Printability Device" used for the rigid-channel printability sweep (see Section 3.1). Perspective view shows the two-edge-supported bridging condition of the channel roof, which spans between two solid sidewalls with the front and back faces left open. Cross-sectional view shows the channel lumen width (W) and roof thickness (t) as imaged by the microscope. Top view confirms that the roof is supported only along its two lateral edges (solid lines) while the front and back edges are free (dashed lines); (B) "Functionality Device" — a Quake-style membrane valve — used for membrane functionality testing (see Section 3.2). Perspective view shows the monolithic block geometry with an enclosed control chamber (upper, semi-transparent front wall shown as dashed to reveal interior) and an open-face flow channel (lower). The membrane is the single thin slab at the boundary between the two regions. Cross-sectional view shows the stacked configuration with applied control pressure (P) acting downward on the membrane toward the flow channel; the doormat is an optional sealing feature introduced in Section 3.3. Top view shows the membrane with the control chamber omitted for clarity; the membrane perimeter is clamped from above by the surrounding control-chamber walls (labeled supported edges), while beneath it the flow channel retains free front and back faces as in row A.*

The device geometries were defined using scalar parameters corresponding to channel width, channel height, membrane thickness, chamber geometry, and sealing features. These parameters were treated as global variables and systematically varied to generate families of related test structures. For each study in the framework, selected parameters were swept across predefined ranges while others were held constant. Resulting geometries were arranged into arrays and exported as single STL files, allowing all variants within a sweep to be fabricated in a single print under identical conditions. The same parametric scripts were then reused across all experiments, with only parameter ranges modified between studies.

Because prior work[57] on light-based microfluidic printing has shown that defining features in discrete pixel increments improves geometric fidelity relative to sub-pixel feature definitions that require interpolation during slicing, the geometries in this study were parameterized directly in printer quanta. Specifically, all dimensions were expressed as integer multiples of the printer pixel size in the lateral direction and the layer thickness in the vertical direction. This choice also supports the central goal of the proposed framework: designs defined in printer quanta can be transferred between printers or resins without introducing additional geometric interpolation artifacts during slicing. Accordingly, both physical dimensions (μm) and printer-quantized units (pixels or layers) are reported throughout this study.

For the initial parametric sweeps, the channel height of the flow geometry was fixed at 250 μm (5 printed layers) as a practical starting value informed by representative 3D-printed membrane-valve geometries reported in the literature,[6, 47] both of which used approximately this same channel height in their baseline designs. Specifically, these prior examples were selected because they were fabricated on commercial printing platforms, making them closer to the present workflow than studies based entirely on custom hardware. The present study therefore did not treat 250 μm as a theoretically optimal or minimum channel height, but as a literature-informed starting value for the initial parameter-space exploration.

Notably, both prior valve designs relied on localized sealing mechanisms rather than full-width channel occlusion. In the valve reported by Rogers et al.,[47] closure occurs through localized Plunger-style blockage, whereas in the Quake-style valve reported by Lee et al.,[6] a raised seat—herein referred to as a doormat—similarly localizes membrane contact during sealing. Therefore, these prior examples motivate not only the starting height, but also the recognition that practical membrane-valve geometries need not rely on full-width or full-depth occlusion.

2.4. Printer and Exposure Settings

All test structures were fabricated using an Asiga Ultra DLP 3D printer (Asiga, Sydney, Australia) with a 32 μm pixel resolution. The printer is equipped with a 385 nm UV LED light engine and supports an open-materials architecture, enabling the use of third-party commercial resins without modification to the hardware or print workflow. Prints were performed in an Asiga UltraGloss vat, which provides a smooth optical interface for membrane and channel fabrication.

For NanoClear, exposure parameters were selected from the Asiga Material Library, and all prints were carried out using these manufacturer-recommended settings except for a few modifications. Specifically, the layer thickness was 50 μm, and the anti-aliasing, Z-layer compensation, 4K, and transparent print modes were disabled for all prints in this study. No custom curing profiles, grayscale modulation, or multi-material steps were used.

For Dental IBT, the same approach was applied: all prints used the default Asiga Material Library settings for that resin, subject to the same modifications described above for NanoClear.

2.5. Post-Processing

Following 3D printing, unpolymerized resin was initially removed from each device by manually applying vacuum to the pneumatic and fluidic ports, followed by carefully flushing the interiors of the valves and flow channels with isopropyl alcohol (IPA). A second vacuum application was then performed to extract residual IPA from the devices. This process was repeated 3 times to ensure all uncured resins are removed from the negative features. The devices were subsequently optically cured by placing them in a custom curing station for ~3 minutes. This curing station is a stock AsigaFlash station (Asiga, Australia).

2.6. Microscopy

Visualization of fluid flow and valve functionality was performed using a Microqubic 3D MRCL700 microscope (MicroqubicAG, Feldpark 29, 6300 Zug, Switzerland), with transmitted (brightfield) light source, and the stock "medium zoom" #2 lens from the manufacturer for all devices, unless indicated otherwise. The images and videos were subsequently improved via ImageJ Fiji software by correcting for uneven illumination via background subtraction, and by enhancing contrast[58].

2.7. Image Analysis

Transmitted-light microscopy images were analyzed using a custom MATLAB pipeline across two distinct workflows corresponding to the printability and functionality stages of the framework.

2.7.1. Lumen-State Classification

As-printed cross-sectional images without actuation were used in both, the Printability (see Section 3.1.1) and the Functionality (see Section 3.2), sweeps to obtain the open state lumen mask of the microfluidics channel mimicking devices. No image registration between states was required. For each image, the open-state lumen boundary was segmented using the Segment Anything Model (SAM)[59], which was supplied with a center-point prompt targeting the middle of the channel cross-section. Candidate lumen masks were accepted only when they showed an enclosed-region intensity response greater than that of nearby solid material, evaluated for both bright-lumen and dark-lumen contrast cases, and were spatially consistent with the intended channel location.

Channel lumen outcomes were then classified into three states: *not formed*, defined as absence of a resolved lumen at the intended channel location; *occluded*, defined as a channel structure with partial or complete lumen narrowing; and *open*, defined as a continuous bright negative-space lumen. A fourth outcome, touchdown — a roof that prints and remains attached to the sidewalls but rests on the channel floor, leaving no open lumen — was recorded where it occurred (see Section 3.1.1). Top-view images were used to confirm lumen continuity along the channel length where cross-sectional appearance alone could not exclude longitudinal collapse. These outcomes were used to construct the lumen-state maps in Section 3.1.1.

For the printability sweep geometries, printed *sag* was additionally extracted from the same as-printed images. The sag was defined as the downward displacement of the lowest point of the suspended membrane into the channel lumen, expressed as a percentage of the nominal channel height (see Figure 2A).

2.7.2. Membrane Deformation Metrics

Membrane deformation metrics for the functionality analysis (see Section 3.2) were extracted from paired open-state and closed-state (inflated) cross-sectional images. SAM was applied exclusively to the open-state image using the same center-point segmentation procedure described above, producing a reference lumen mask that defined both the open lumen footprint and the nominal channel height for all subsequent measurements. The closed-state image was then rigidly registered to the open-state image, with the estimated transform accepted only when it measurably improved image agreement, and photometrically normalized to the open-state image to compensate for frame-to-frame illumination differences prior to comparison.

Obstruction was identified within the reference lumen mask by computing a normalized pixel-intensity-loss map between the registered closed-state image and the open-state image. Pixels within the reference lumen mask whose intensity decreased beyond a data-adaptive threshold were identified as membrane-occupied. To prevent spurious detections in the absence of genuine membrane motion, the in-lumen intensity-loss statistics were compared against a static reference region within the same image pair, and pairs lacking a significant excess were assigned a closure of zero; detections inconsistent with a wall-anchored membrane profile were likewise rejected by automated plausibility checks. For each image column, the obstructed region was defined as the extent from the open-lumen top boundary down to the deepest membrane-occupied pixel in that column, intersected within the reference lumen mask. Two metrics were then extracted from this obstruction map as shown in Figure 2:

Membrane reach was defined identically to printed sag — the vertical position of the lowest point of the membrane expressed as a percentage of nominal channel height — but measured from the inflated-state image rather than the as-printed image (see Figure 2A). Reach was extracted by fitting a circular arc to the column-wise depth profile of the obstruction front within the trimmed central region of the channel, consistent with the circular-arc membrane approximation adopted in Section 3.3.3, with the arc apex taken as the maximum reach point. A constrained parabola and, failing that, a geometric maximum were used as fallbacks when the arc fit was invalid.

Area obstructed was defined as the fraction of the reference lumen mask occupied by the deflected-membrane profile, computed from the same wall-anchored arc fit used for reach, and reported as a percentage of the total open-state lumen area (see Figure 2B). All conditions were measured on n = 3 replicate devices and are reported as mean ± standard error of the mean (SEM).

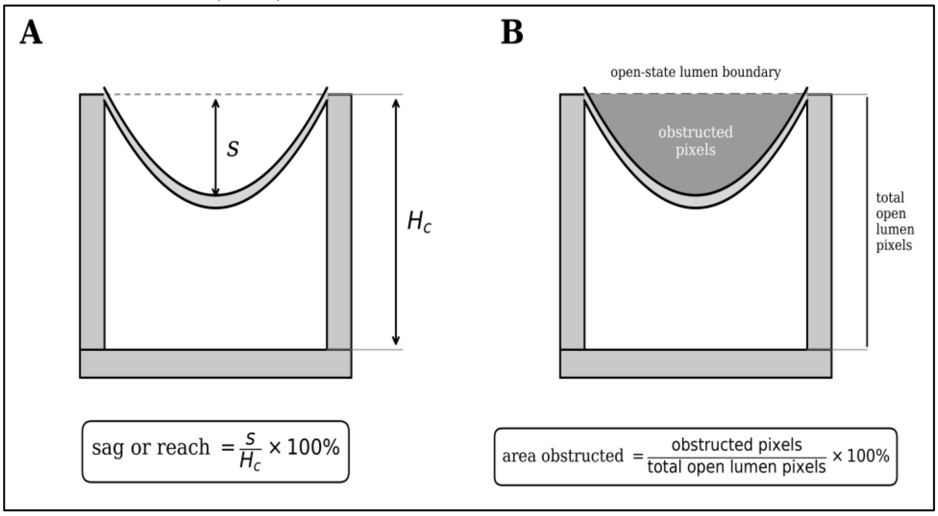

Figure 2 Geometric definitions of membrane deformation metrics used for functional analysis. *(A) Cross-sectional schematic showing channel height (Hc), the downward displacement of the membrane's lowest point (s), and the corresponding sag or reach value expressed as s/Hc × 100%. The same measurement is termed printed sag when evaluated in the as-printed state and membrane reach when evaluated after inflation. (B) Cross-sectional schematic showing the open-state lumen footprint (dotted line = upper boundary) and the fraction of that footprint blocked by the membrane after deformation (shaded), corresponding to area obstructed.*

Note that the two metrics are measured on different device types: as shown in Figure 1, printed sag is characterized on the two-edge-supported Printability Device (roof supported only by the sidewalls), whereas membrane reach is measured on the Functionality Device, whose membrane perimeter is additionally clamped from above by the control-chamber walls (see Section 2.3). The two are therefore not directly comparable, and the implications of the roof-sag values are taken up in Section 3.1.2. Note also that both device types require sidewalls thick enough to act as effectively rigid supports: slender walls can tilt inward under the load of the spanning roof, which alters the effective width and biases both metrics. Wall thickness was therefore kept well above the minimum printable feature size in all devices reported here.

2.8. Valve Performance and Durability Characterization

Burst testing was performed on complete flow devices spanning channel widths of 60 to 120 printer pixels. The control (valve) pressure was increased stepwise from 10 to 60 psi in 10 psi increments, holding each step for 60 s, with three replicate devices per width. Membrane failure was identified visually as dye breakthrough between the control and flow layers: upon failure, air from the pressurized control chamber blows the dye out of the flow channel. Failure events were imaged on the Microqubic MRCL700 (low-zoom lens, top-down view, transmitted back-lit illumination).

Flow-blocking efficiency was quantified as the flow rate through the closed valve expressed as a percentage of the open-valve flow rate under identical driving conditions, such that 100% leakage corresponds to an entirely ineffective valve and 0% leakage to complete blocking. Visualization measurements used water with 10% (v/v) food dye as the working fluid, while quantitative flow measurements used pure water; flow was driven at a constant 3 psi. Blocking was assessed visually by image analysis and quantitatively by pipette measurement of the delivered volume (n = 3 replicate devices). Efficiency was recorded as a function of control pressure for each channel width.

Cyclic durability was assessed by actuating valves through 1,000,000 open/close cycles at 30 psi and 5 Hz, using computer-controlled solenoid valves (custom driver hardware, AltVIVO, Inc.); the actuated on-chip valves were recorded by time-lapse imaging every 5 s throughout the run. Device integrity was verified before and after cycling in two ways: qualitatively, by dye filling and microscopy while actuating the valve under the cycling conditions with a 60 s hold; and quantitatively, by re-measuring the blocking efficiency using the protocol described above.

On-chip pump performance was characterized by measuring the displaced volume per actuation cycle and the resulting net flow rate as functions of actuation frequency. The pump was driven by actuating three valve chambers in a six-phase peristaltic sequence (valve states 1-2-3: on-off-off, on-on-off, off-on-off, off-on-on, off-off-on, on-off-on), with 0.2 s per phase and therefore 1.2 s per full cycle, at a control pressure of 30 psi. Delivered volume was measured by pipette and converted to a net flow rate (volume per unit time). A 10 mL syringe barrel served as an open reservoir and a 10 mL glass bottle as an open collector, connected by equal 20 cm lengths of 1/16 in. OD × 1/32 in. ID tubing with 23G needles for the tubing-to-device connections; back-pressure testing was not performed. These conventions follow characterization practice established for 3D-printed membrane micropumps [6].

3. Results and Discussion

3.1. Stage I — Rigid-Channel Printability Sweep

The initial step of the geometry-first framework is a rigid-channel printability sweep, whose purpose is to establish a parameter window within which enclosed channels can be fabricated reliably for a given printer–resin combination before additional requirements—such as suspended membranes, membrane compliance, or valve closure—are introduced. The Printability Device makes this screening step deliberately cheap: it is passive — requiring no control chamber, pneumatic tubing / plug-in needle interfacing with the device, or electronics-driven or manual pneumatic actuation — it consumes less material than a complete valve, and it arrays compactly so that an entire width-thickness sweep can be fabricated in a single print and observed easily via optical microscopy or other imaging modalities. Because the front and back faces are open, the spanning roof is carried only along its two lateral edges (see Figure 1A), so the sweep probes each width in its least-supported, worst-case bridging condition. It thus serves as a disposable screening coupon for newly adopted resins, whose passive deformation map, as shown in Section 3.2, foreshadows the width range within which actuated membranes remain functional.

To determine this window, simple enclosed channels (Printability Devices in Figure 1) were fabricated in NanoClear under fixed default Asiga settings and evaluated after the complete fabrication workflow, including printing, solvent clearing, and post-curing. At this stage, the objective is only to determine whether enclosed channels can be fabricated cleanly under the selected procedures. Valve actuation and membrane functionality are intentionally not considered yet; instead, those are evaluated in later stages of the framework. The present step therefore focuses solely on whether an intended negative-space channel can be produced without obstruction and deformation.

In this part of the study, channel width and roof (i.e., the valve membrane) thickness were varied parametrically, with width spanning from 32 to 4,800 μm (i.e., from 1 printer pixel to 150) and roof thickness spanning from 50 to 500 μm (i.e., from 1 printed layer to 10; the number of printed layers forming the roof, and later the membrane, is abbreviated ML, for "membrane layers", in the figures and text that follow). The channel height was chosen to be 250 μm (5 printed layers) as discussed in Section 2.3.

3.1.1. Lower Width Limit of Enclosed-Channel Formation

To determine the minimum printable enclosed channel width under the selected printing conditions, lumen state was assessed using transmitted-light microscopy with back-illumination so that the presence or absence of a resolved lumen could be identified directly from optical contrast. Representative examples are shown in Figure 3, where the top row shows cross-sectional images and the bottom row shows the corresponding top views used to verify the longitudinal channel condition along the device.

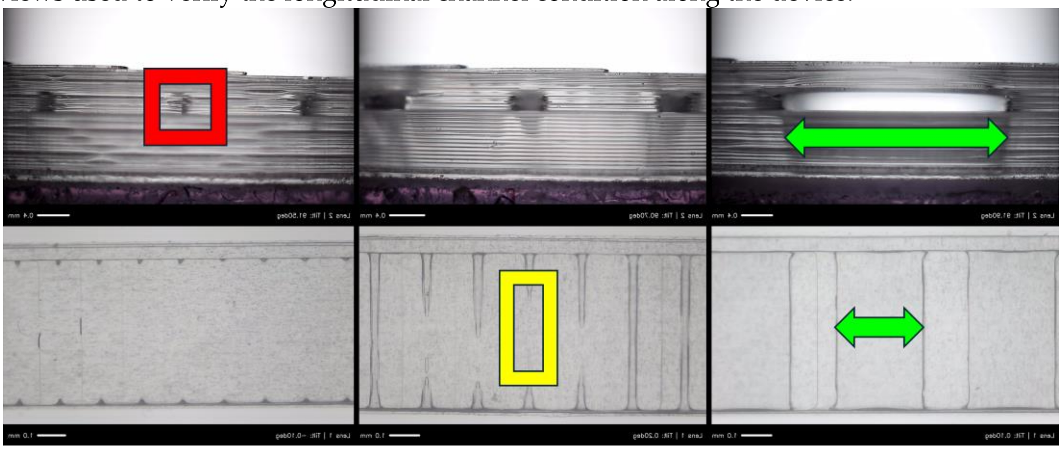

Figure 3 Representative transmitted light microscopy views of the Printability Device used for lumen-state classification. *The top and bottom rows show cross-sectional and corresponding top views (used to confirm the longitudinal channel condition), respectively. Each column illustrates a different fabrication outcome observed during the printability sweep: LEFT- "Not Formed" (red box marks the intended channel location); CENTER – "Occluded" (yellow box shows the source of channel occlusion); RIGHT – "Open" (green arrow shows the channel width correspondence between the top and bottom row images). Scale bars: top row, 0.4 mm; bottom row, 1 mm.*

Across the parametric sweep, four reproducible outcomes were observed: 1) In the *not-formed* condition, no true lumen is visible in cross-section and the intended channel location appears as resin-filled material or only a faint outline of the feature (red box in the top-left panel of Figure 3); 2) In the *occluded* condition, a channel structure is present but the lumen appears dark or partially dark in cross-section, indicating narrowing or blockage of the negative space. Top-view imaging further reveals a characteristic lumen-"pinching" mode in which opposite channel walls approach most strongly near the *lengthwise midpoint of the channel* (yellow box in the bottom center panel of Figure 3). Similar dark-lumen states have been reported previously in projection-based vat-photopolymerization studies of enclosed microchannels and are attributed to shrinkage-driven wall deformation and local overcuring.[5, 60-62] However, in the present study exposure parameters were intentionally held fixed so that lumen closure behavior could be evaluated as a function of geometry alone, consistent with the objective of identifying valve-feasible design regimes through geometric modification rather than printer-specific process tuning; 3) In the *open* condition, the lumen appears as a bright continuous negative-space region in cross-section and corresponds to a continuous channel in the top-view image (green arrows in the right column panes of Figure 3); and 4) In the touchdown condition, observed only for single-layer roofs at the largest widths (≥ 90 px), the roof prints and remains attached to the sidewalls but sags through the full channel height and rests on the channel floor, leaving no open lumen (purple cells in Figure 4).

After establishing these image-based outcome categories, the full parametric sweep was summarized as a categorical lumen-state map shown in Figure 4. Each geometry in the sweep was fabricated in triplicate, and each condition was assigned according to the 'majority wins' state across the three replicates.

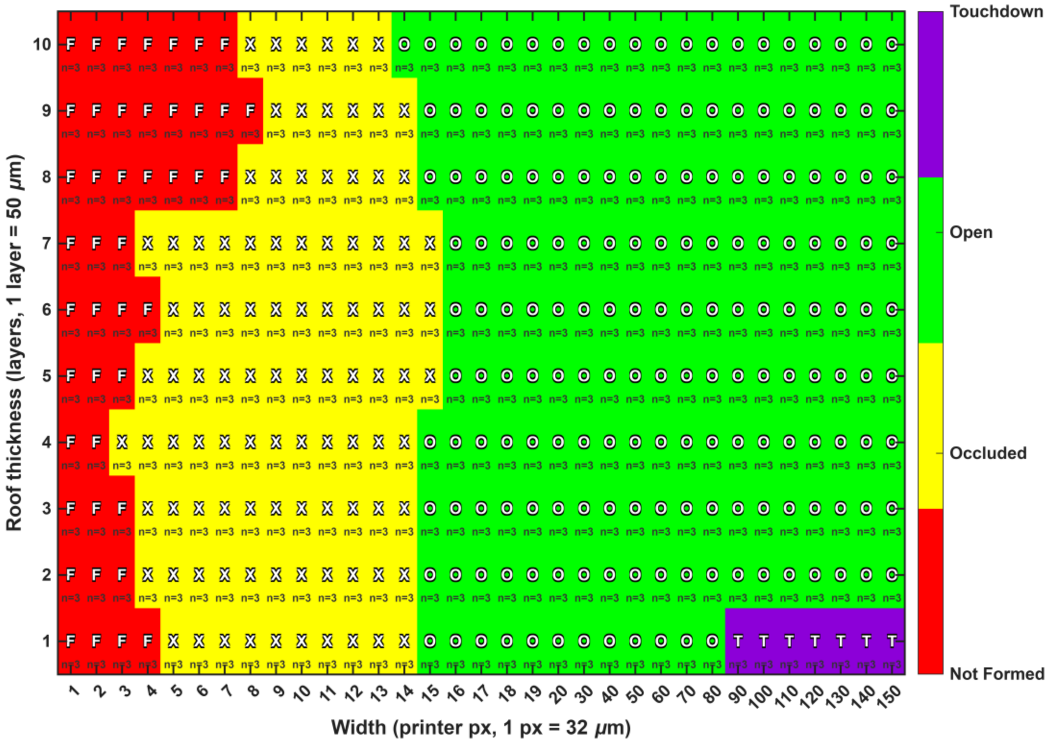

Figure 4 Rigid-channel lumen-state map for NanoClear at a fixed channel height of 250 µm (5 printed layers) under default Asiga settings, spanning channel widths of 1-150 printer pixels (0.032-4.8 mm) and roof thicknesses of 1-10 print layers (50-500 µm). *Each cell shows the majority lumen state across triplicate prints (n = 3). Four regimes are observed: a "not-formed" regime at the smallest widths; an "occluded" transition regime at intermediate widths; an "open" lumen regime at sufficiently large widths; and, for single-layer roofs at widths ≥ 90 px, a "touchdown" regime in which the roof prints and remains attached to the sidewalls but collapses fully onto the channel floor, leaving no open lumen. The map defines the printability bounds for rigid enclosed channels used to constrain the next stage of the framework.*

The resulting state map i**Figure 4**dentifies the boundaries between the *not-formed*, *occluded*, and *open* outcomes across the width–thickness parameter space for the fixed-channel-height NanoClear study. The "hard" lower limit of channel formation corresponds to the onset of the *not-formed* regime, where the intended channel region polymerizes as a nearly solid volume and no mechanically stable lumen develops. In contrast, the *occluded* regime represents a practical or "soft" minimum width threshold, since partially pinched lumens in this regime may in some cases be recovered through improved cleaning, post-processing, or exposure optimization, although such process-parameter tuning was intentionally excluded from the present geometry-driven framework. Accordingly, a conservative minimum printable width of approximately 480 µm (15 pixels) was adopted as the admissible lower bound for subsequent valve-geometry studies. The state map therefore defines the admissible starting region for the suspended-membrane studies that follow. Having established the conservative lower bound for enclosed-channel formation under fixed printing conditions, the next step in the framework is to identify the corresponding upper geometric limit imposed by roof-width stability, which defines the maximum printable enclosed channel width examined in Section 3.1.2.

3.1.2. *Upper Width Behavior of Enclosed Channels (Roof Sag)*

After establishing the conservative *lower* bound for enclosed-channel formation, the next step in the rigid-channel feasibility framework was to examine whether an *upper* geometric limit exists for the printable width of enclosed channels under the same fixed printing conditions. To that end, channel width was progressively increased while varying the number of printed layers forming its roof, and the resulting structures were evaluated for roof "sag" (defined in Section 2.7.1) using cross-sectional microscopy.

As expected, the sag increased with larger channel width and thinner roof sizes (see Figure 5): with the most pronounced sag occurring for roof thicknesses of 50-150 µm (i.e., 1-3 printed layers), while at thicknesses >3 printed layers the roofs exhibited no visible sag regardless of channel width.

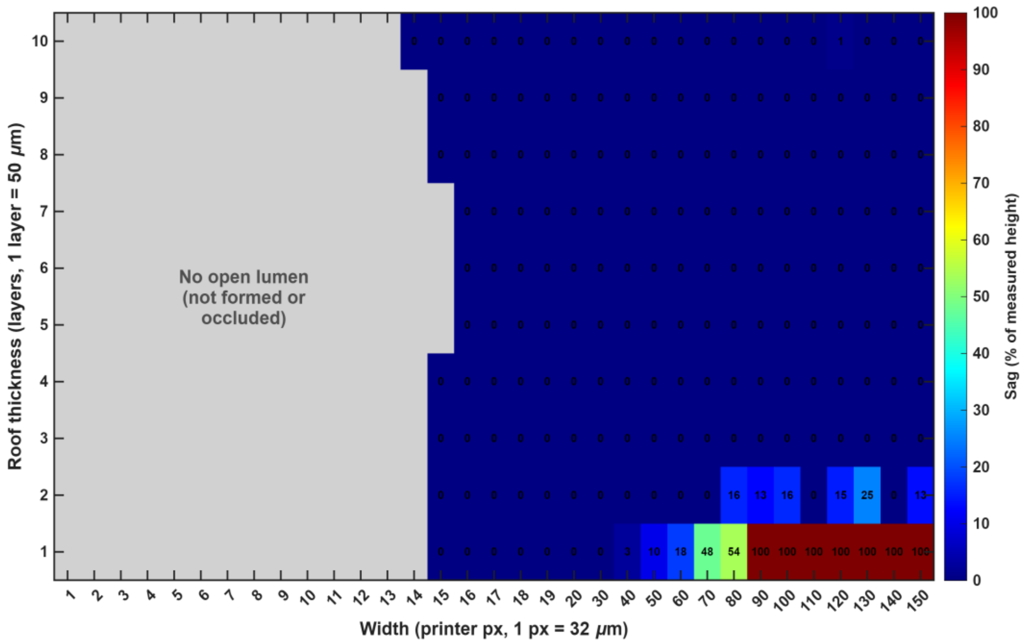

Figure 5 Quantitative membrane roof sag across the width-thickness design space. *Median roof sag of the printed membrane (n = 3 replicate prints per cell), expressed as a percentage of the measured lumen height, for the same design space as Figure 4 (constant channel height H = 5 layers; x-axis: channel width in printer pixels, 1 px = 32 µm; y-axis: roof thickness in print layers, 1 layer = 50 µm). Sag was quantified only where an open lumen was present; gray cells mark combinations with no open lumen (channel not formed or occluded), corresponding to the not-formed and occluded regions of Figure 4. Cells classified as membrane touchdown in Figure 4— where the roof collapsed fully onto the channel floor — are plotted as 100% sag, the full-height*

deflection limit. At the thinnest roof (ML = 1, 50 µm) sag increases sharply with channel width, from ~3% at 40 px (1.28 mm) to full touchdown (100%) at ≥ 90 px (2.88 mm), whereas roofs of three or more layers (≥ 150 µm) exhibit negligible sag across all widths, confirming that roof thickness — not channel width — governs sag resistance. Sag is measured from cross-sectional images using a corner-baseline reference.

Importantly, within the swept width range (up to 4,800 µm, i.e., 150 printer pixels), no discrete loss of enclosure was observed: increasing channel width produced a gradual transition from nearly flat roofs to strongly sagged roofs rather than a loss-of-formation boundary analogous to the lower-width not-formed regime identified in Section 3.1.1. For single-layer (50 µm) roofs the progression is steep: sag grows from ~3% of the lumen height at 40 px to ~48-54% at 70-80 px, and from 90 px onward the roof undergoes complete touchdown (100% sag, roof resting on the channel floor) at every tested width through 150 px. Two-layer roofs sag only partially (~13-25%) over the same range, and roofs of three or more layers remain essentially flat, confirming that roof thickness — not channel width — governs sag resistance. These passive observations provide the geometric backdrop for Stage II: the enclosed-channel test structures fail conservatively — touchdown from 90 px — whereas the complete valve devices of Section 3.2 remain functional to 140 px. The sag map therefore serves as a conservative, quick-to-measure screen for the widths at which membrane collapse becomes the dominant failure risk, and the valve-format failure at 150 px (see Section 3.2) shares the same pre-sag mechanism that the map first detects at 90 px.

As noted in Section 2.7.2, however, this roof sag is measured on the Printability Device, whose roof is carried only by the two channel sidewalls with entirely free front and back edges (see Figure 1); the valve membranes of the later stages are additionally clamped around their perimeter from above by the control-chamber walls and are therefore expected to deform less than the bare roofs measured here. Consistent with this free-edge boundary condition, the largest sag occurred near the open longitudinal channel ends rather than uniformly along the channel length, and the cross-sectional measurements therefore capture the maximum, worst-case deformation within the channel width rather than a spatially uniform longitudinal profile. The sag measurement itself is mechanism-agnostic: the end-state deformation recorded here may combine contributions from print-through over-curing at the roof underside, gravity-driven slumping of the not-yet-fully-cured span, and capillary loading during post-print draining and washing of the enclosed channel. The framework deliberately does not attempt to separate these contributions, because every downstream design decision depends only on the as-fabricated geometry that the sweep records, whatever its origin. The roof-sag map is thus a conservative indicator, and its ability to predict the membrane's functional behavior was investigated directly in the next stage of the framework.

3.2. Stage II — Membrane Functionality Testing

After Stage I established which suspended-membrane geometries could be fabricated reliably within the envelope mapped in Figure 4 and Figure 5, the next question was whether the resulting membranes were functionally suitable for valve operation. In particular, Section 3.1.2 showed that enclosed-channel roofs exhibited progressively increasing sag with increasing channel width under identical printing conditions — culminating, for single-layer roofs, in complete passive touchdown from 90 px onward, with no discrete loss of enclosure anywhere in the swept range. Whether this escalating deformation carries functional consequences therefore remained unresolved and was examined directly in this stage using the Functionality Devices from Figure 1.

Consequently, two functionality metrics (defined in Section 2.7) were measured during membrane actuation to evaluate closure performance across the tested width range: membrane 'reach', which quantifies how deeply the membrane extends toward the channel floor during inflation; and 'obstructed area', which quantifies how much of the lumen footprint becomes blocked (see Figure 6).

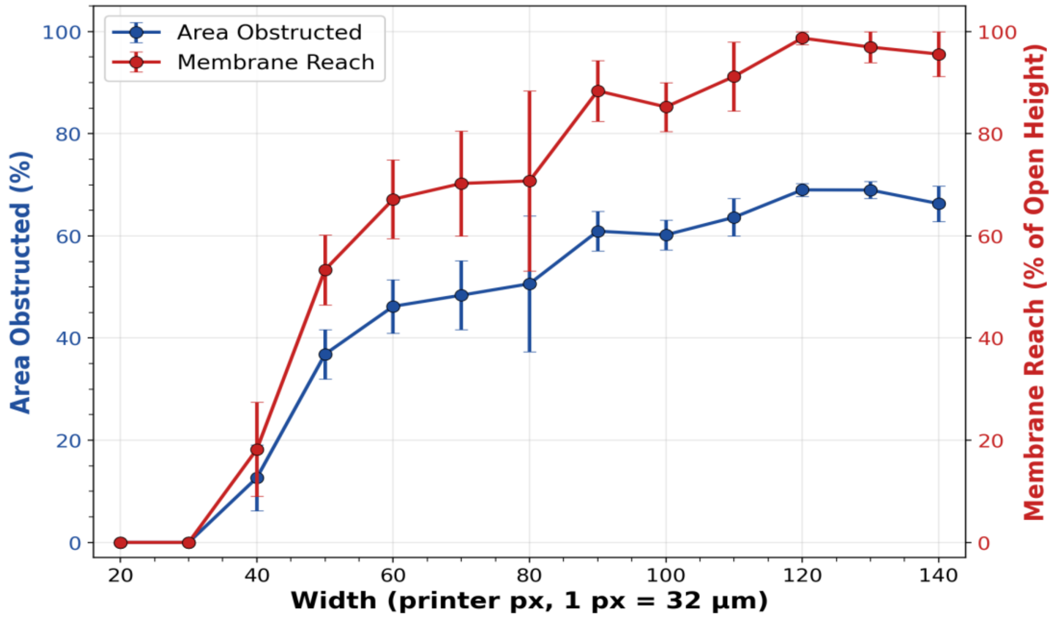

Figure 6 Relationship between obstructed area (blue, left axis) and membrane reach (red, right axis) as a function of channel width, for single-layer membranes (ML = 1) at the baseline channel height of five printed layers (250 µm). *Area obstructed is the percentage of the original open-state lumen footprint blocked by the membrane in top view; membrane reach is the vertical position of the membrane apex relative to the channel floor, expressed as a percentage of channel height. Symbols and error bars denote mean ± one standard error of the mean (n = 3 replicate devices). The series extends to 140 px, the widest width at which devices remained functional; 150 px devices are excluded because their roofs pre-sag past the printability limit, leaving the open and closed states indistinguishable (see Figure S1). Corresponding measurements for thicker membranes (ML = 2, 3) and for a doubled channel height (H = 10 layers) are provided in the ESI (see Figures S2 and S3).*

Both membrane reach and obstructed area increased with channel width, approaching values consistent with near-complete closure at widths ≥ 80px (2560 µm) for single-layer membranes (Figure 6). Membrane reach rose approximately linearly with width before saturating near 100% of the channel height once the membrane contacted the channel floor. This linear-rise-then-saturation behavior indicates that deflection grows in proportion to channel width over most of the range — a relationship formalized later as the basis of the geometric closure framework (see Section 3.3.3) — with the plateau reflecting the geometric ceiling imposed by floor contact rather than a breakdown of the underlying scaling. The same behavior was observed for thicker membranes and for a doubled channel height, with the corresponding graphs and measurements provided in the ESI (see Figures S2 and S3): thicker membranes rose along the same trend but more slowly, and began to deflect measurably only at larger widths (onset widths $W_0 \approx 16$, 44, and 64 printer pixels for one-, two-, and three-layer membranes, respectively), which constitutes a practical design constraint, since it sets the minimum channel width at which a given membrane recipe can actuate at the operating pressure. Doubling the channel height (H = 10 layers, 500 μm) left the rise essentially unchanged apart from a larger onset width ($W_0 \approx 38$ px), indicating that the rate at which deflection grows with width is set by the membrane and the printing process rather than by the channel. These reach measurements are the raw input to the geometric closure framework of Section 3.3.3, where the slope of this rise is formalized as the membrane deflection coefficient κ and used to prescribe sealing geometry; the fitted values are reported there rather than here. Because Section 3.1.2 showed that roof sag in the Printability Devices increased over this same width range — with the sharp single-layer sag rise near 90-100 px foreshadowing the pre-sag collapse that ultimately terminates valve function at 150 px (below) — these results indicate that the passive sag map served as a useful predictor of the widths at which the inflated membranes begin to achieve effective channel closure. In this sense, the rigid-channel sag measurements in Figure 5 provided an indirect geometric indicator of valve functionality (i.e., membrane closure potential) under the same fabrication conditions.

Importantly, the suspended-membrane valve devices used for functionality testing in this section did not exhibit visually detectable sag in the open state prior to actuation anywhere within the functional width range (see Figure 8 **Cross-sectional transmitted-light microscopy images of a suspended-membrane (Quake-style) valve8**-LEFT). This indicates that the improved closure observed at larger widths cannot be attributed to pre-existing lumen obstruction in the open configuration. Instead, the sag observed in the enclosed-channel test structures of Section 3.1 appears to reflect a fabrication-dependent deformation tendency associated with free-edged channel roofs, which becomes functionally consequential only at the largest widths once the membrane is actuated. This same roof deformation ultimately bounds the closure characterization at the upper end — as a data-discovered limit rather than a hardwired cutoff: at 4,800 μm (150 printer pixels) the channel roof pre-sags so severely that the open-state lumen is already collapsed, leaving no open baseline against which membrane reach can be defined. Cross-sections of Functionality Devices at 150 px confirm this directly — the open (unactuated) and closed (actuated) states are visually indistinguishable (see Figure S1). Accordingly, trailing non-functional widths are excluded from Figure 6 by a per-series rule (the terminal run of non-functional devices is dropped), and the demonstrated functional range currently extends to 140 px (~4.5 mm) for the single-layer, H = 5 series. The contrast with the enclosed-channel printability structures — whose single-layer roofs touch down passively from 90 px (see Section 3.1.2) — underscores that the printability sweep is a conservative screen: the valve-format devices, whose membranes gain support from the surrounding valve structure, remain open and functional well beyond that width.

To make this predictive relationship explicit, Figure 7 aligns the passive printability regimes of the rigid-channel sweep (flat roof, partial sag, touchdown) with the actuated functionality regimes of the corresponding valve devices (no actuation, partial actuation, strong closure, collapse at rest) for each membrane thickness across the full width range. Three practical rules emerge. First, sag is a compliance indicator rather than a defect: the onset of measurable sag in the rigid sweep (~50 px for single-layer membranes) coincides with the onset of strong closure in the valves, while membranes that never sag (three layers and thicker) remain stiffness-limited throughout. Second, touchdown in the rigid sweep does not mark valve failure: single-layer roofs touch down from 90 px onward, yet the corresponding valves remain functional through 140 px — a safety margin of roughly 60 px (~1.9 mm) between the passive warning and true functional failure at 150 px. Third, the map extrapolates to untested territory: two- and three-layer membranes never touch down anywhere in the 150 px sweep, predicting that their functional windows extend beyond the 100 px reached in valve testing. The inexpensive passive sweep thus brackets the functional window from both ends — flagging stiffness-limited membrane recipes at narrow widths and collapse-limited ones at wide widths — before any valve is fabricated. This stiffness limit is a property of the resin as much as of the geometry: NanoClear is a rigid, non-flexible photopolymer that was not developed for compliant structures, and to our knowledge had not previously been used for microfluidic valves at all; usable membrane flexure was obtained only at the thinnest printable roof, a single 50 μm layer, which is why the single-layer recipe is the one carried through the remainder of this study.

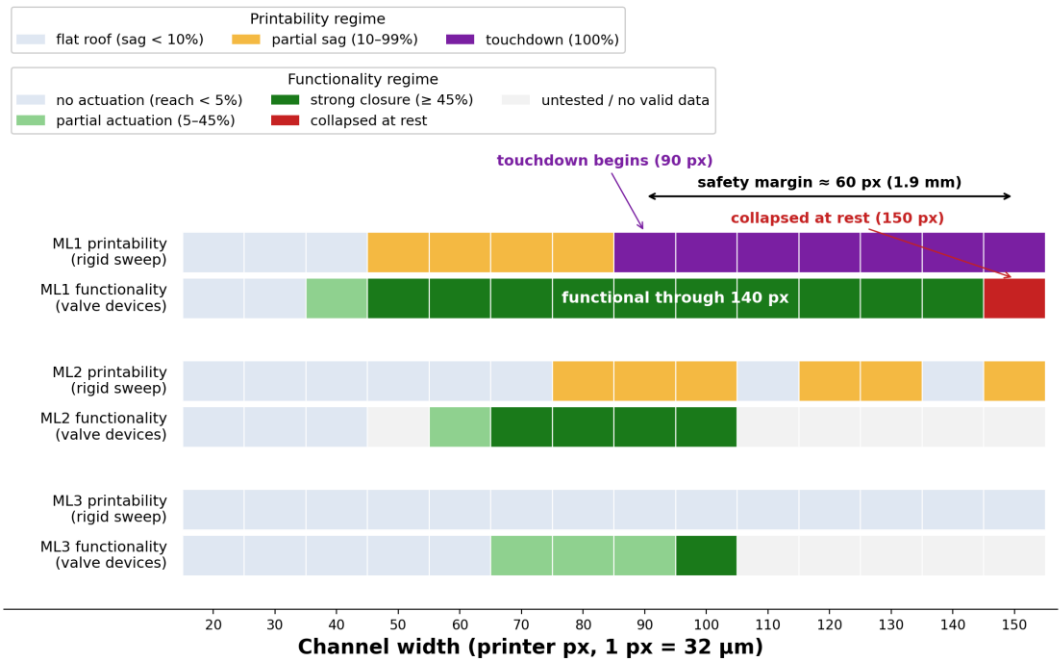

Figure 7 Regime correspondence between passive printability and actuated valve functionality. *For each membrane/roof thickness (ML = 1-3; H = 5 layers), the upper band shows the printability regime from the rigid enclosed-channel sweep (flat roof: sag < 10%; partial sag: 10-99%; touchdown: 100%) and the lower band shows the functionality regime from the corresponding valve devices (no actuation: reach < 5%; partial actuation: 5-45%; strong closure: reach $\geqslant$ 45%; collapsed at rest: open and closed states indistinguishable), as functions of channel width (printer px, 1 px = 32 μm). Light gray cells are untested or yielded no valid measurement. Sag onset coincides with the onset of strong closure; single-layer touchdown (from 90 px)*

precedes functional collapse (150 px) by a ~60 px (~1.9 mm) safety margin; and the absence of touchdown for ML = 2-3 predicts functional windows extending beyond the tested 100 px.

Even within the functional channel-width range, area obstruction remained below 100% despite membrane reach approaching 100%. Cross-sectional imaging of pressurized devices revealed the origin of this residual open area: the geometric mismatch between the approximately part-spherical inflation profile of the membrane and the rectangular channel cross-section leaves triangular void regions in the lower corners of the lumen that the membrane cannot conform to (see Figure 8 **Cross-sectional transmitted-light microscopy images of a suspended-membrane (Quake-style) valve8**-RIGHT). These corner-gaps persist regardless of membrane reach and represent a fundamental geometric incompatibility between the curved inflated membrane and a sharp-cornered rectangular channel floor.

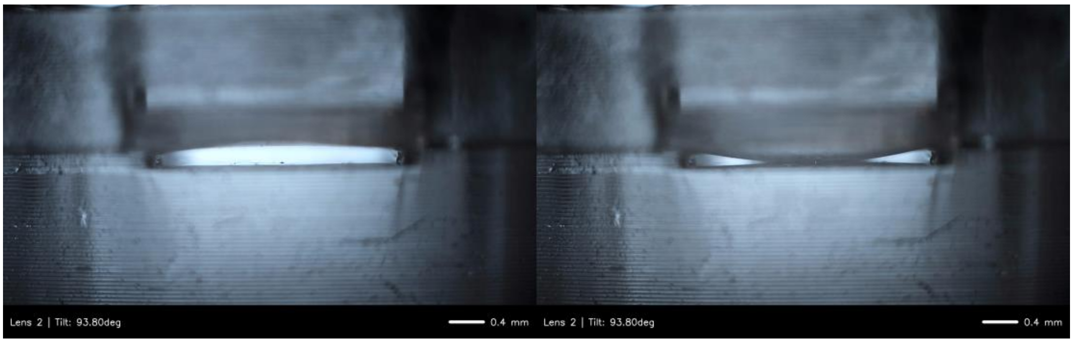

Figure 8 Cross-sectional transmitted-light microscopy images of a suspended-membrane (Quake-style) valve8 at channel width W = 100 printer pixels. *Left: open-state image showing the membrane prior to actuation. Right: pressurized (closed-state) image showing the inflated membrane contacting the channel floor with residual corner gaps. Scale bar: 0.4 mm.*

Both the pre-sag-imposed upper channel-width limit and the persistent corner gaps therefore define the true operating envelope for suspended-membrane valves in NanoClear under the present fixed-parameter workflow. The corner-gap geometry directly motivates the sealing-feature design introduced in Section 3.3.

3.3. Stage III: Channel-Floor Curvature as a Strategy for Suppressing Discretization-Induced Leak Paths

3.3.1. Part-Cylindrical Channel Floors and Contact-Barrier-Limited Sealing

A classical strategy for improving closure of membrane valves is the use of a semi-rounded channel floor. This geometry is standard in soft-lithography implementations of Quake-type valves[11], where elastomeric membranes conform smoothly to semicircular flow channels and achieve reliable sealing across the full channel width.

In projection-based stereolithography, however, the intended smooth channel curvature is approximated by a staircase-discretized profile determined by the layer thickness (see Figure 9A). As a result, membrane contact with the channel floor occurs at discrete points separated by intervening gaps. These gaps arise from geometric incompatibility between the continuous curvature of the inflated membrane and the voxelized approximation of the channel surface, producing a series of residual flow pathways referred to here as *contact barriers*.

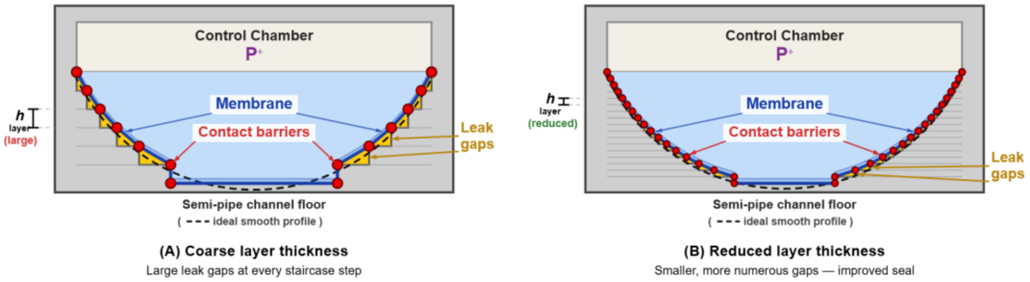

Figure 9 Cross-sectional schematic of a membrane valve with a staircase-discretized semi-pipe channel floor at (A) coarse and (B) reduced layer thickness. *Yellow regions indicate leak gaps between the membrane (blue) and staircase corners; red dots mark membrane–staircase contact points.*

Reducing layer thickness improves conformity between the membrane and the discretized channel floor by increasing the number of contact points and reducing the spacing between adjacent gaps (see Figure 9B). Although this does not eliminate discretization-induced leakage pathways, it increases their hydraulic resistance by shortening their characteristic height and length scales. Alternatively, increasing the channel height-to-width ratio while holding layer thickness constant can also improve membrane conformity, but the effect depends on how the proportions are changed (see Figure S4). Specifically, for a given cross-sectional flow area, using a higher, narrower channel profile reduces the radius of curvature of the floor, which shortens each staircase step and proportionally reduces the area of the leak gaps at every step corner. In contrast, simply increasing channel height without changing width, however, adds steps only in the steeper wall regions where the gaps are already small, leaving the dominant leak pathways along the channel floor essentially unchanged. Additionally, reducing channel width is constrained by the minimum feature size of the printing process and it reduces the membrane's downward reach (i.e., its ability to block the flow). Reducing layer thickness, by contrast, improves seal quality uniformly across the entire channel floor without changing the intended device geometry. Layer thickness is therefore the primary control parameter, with channel cross-sectional proportions offering a secondary means of reducing leakage.

Two practical caveats accompany these geometric levers. At small channel heights, rounded floors create tight wedge-shaped spaces where uncured resin becomes trapped and is difficult to wash out, an issue that likewise affects any recessed curved seat, including the spherical recesses introduced in Section 3.3.2; and at the finest layer pitch (25 μm) the default exposure schedule over-cures negative spaces, partially clogging channels unless the membrane is printed at a coarser pitch (see Section 3.4.2).

The effectiveness of semicircular channel floors in soft lithography therefore reflects both the availability of smooth continuous curvature and fabrication constraints that limit accessible three-dimensional geometries. In stereolithographic printing, where discretization cannot be avoided but arbitrary three-dimensional shaping is readily available, alternative rounding strategies become possible. This motivates the introduction of spherical channel-floor curvature, described in Section 3.3.2, which replaces linear contact-barrier gaps with curved leakage paths that are expected to exhibit higher hydraulic resistance due to their increased length and reduced longitudinal alignment with the flow direction.

3.3.2. Spherical Valve-Seat Geometries for Increasing Leak-Path Resistance

Although part-cylindrical channel floors (like in Section 3.3.1) improve membrane conformity relative to rectangular geometries (like in Figure 8 **Cross-sectional transmitted-light microscopy images of a suspended-membrane (Quake-style) valve8**), the resulting discretization-induced leakage pathways remain predominantly linear and aligned with the channel's flow axis. In projection-based stereolithography, these residual gaps arise from staircase discretization of the curved floor and therefore cannot be eliminated entirely through the cylindrical rounding alone.

An alternative approach is to replace the part-cylindrical sealing interface with a localized part-spherical valve seat[6]. Unlike cylindrical geometries, which can produce discretization-induced leakage pathways that remain continuously aligned along the channel direction, spherical sealing interfaces are expected to disrupt the longitudinal continuity of these pathways by introducing curved and spatially varying contact-barrier geometries, thereby increasing the effective hydraulic resistance to flow.

Conformity to such a part-spherical seat is further improved — though not strictly required — by matching the membrane geometry to the seat. Conventional Quake-style valves employ *rectangular* membranes spanning elongated channels, which deform into barrel-vault-like surfaces; these are naturally matched to part-cylindrical floors (or an inverted-parabolic profile), and pair with a spherical seat only imperfectly (see Figure 10-LEFT). Even so, a spherical seat remains an improvement over no seat at all, because the flexed membrane still settles partially into the recess. Membranes with *circular* deformable regions, by contrast, deform into dome-like surfaces that conform closely to spherical seats and are therefore expected to maximize sealing uniformity across the contact interface (see Figure 10-CENTER & RIGHT). Accordingly, the geometric closure framework developed below treats the circular-membrane/spherical-seat pairing as the best-matched configuration rather than a prerequisite: because the framework operates only on the deflected cross-section of the membrane, it applies equally to a rectangular membrane, which simply seals less uniformly away from the seat center.

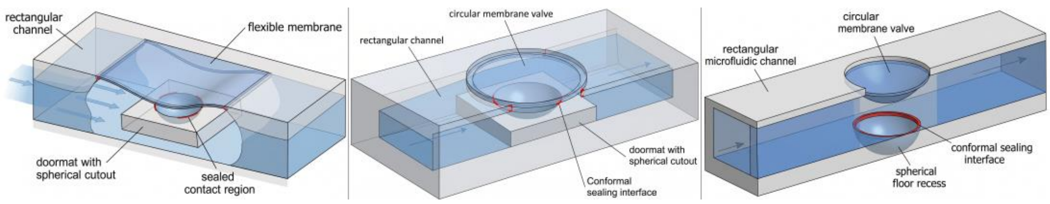

Figure 10 Spherical valve-seat geometries for improving membrane sealing in stereolithographically-printed microfluidic valves. *LEFT - a rectangular membrane is poorly matched to a part-spherical valve seat, producing incomplete conformity at the sealing interface; CENTER - a circular membrane valve paired with a raised doormat containing a spherical cutout, which brings the spherical sealing surface closer to the membrane; RIGHT - a circular membrane valve paired with a part-spherical recess integrated directly into the channel floor, eliminating the raised in-channel obstruction. Red outlines indicate the intended membrane–seat contact region.*

Specifically, two possible implementations of the spherical valve-seat are possible: In the first configuration, the spherical sealing interface is elevated above the channel floor using a raised "doormat" structure that reduces the required membrane vertical travel distance but introduces an upward obstruction within the flow path that locally constricts the flow cross-section, at the cost of added pressure drop and, for particle-laden fluids, a clogging risk (see Figure 10-CENTER). In the second configuration, the spherical seat is recessed directly into the channel floor as a part-spherical cavity (see Figure 10-RIGHT), eliminating protruding in-channel structures but requiring either sufficient membrane reach or a shallower channel to achieve conformal contact with the recessed sealing interface.

Although spherical valve-seat geometries are expected to reduce discretization-induced leakage by disrupting continuous longitudinal flow paths, effective closure additionally requires geometric conformity between the deflected membrane and the sealing interface. This introduces a coupled relationship between membrane curvature, membrane reach, channel dimensions, and valve-seat geometry that motivates the generalized framework developed in Section 3.3.3.

3.3.3. Geometry-Derived Closure Framework and Interactive Design Tool

The preceding sections demonstrate that membrane-valve closure in stereolithographically printed microfluidic devices depends not only on membrane deflection magnitude, but also on geometric conformity between the deflected membrane and the sealing interface. While part-cylindrical and spherical channel-floor geometries can reduce the continuity of discretization-induced leakage pathways, effective sealing additionally requires that the membrane reach and conform to the intended valve-seat geometry. This relationship introduces a coupled geometric constraint linking membrane curvature, channel dimensions, and sealing-feature position.

To generalize these relationships beyond the representative geometries illustrated in Figure 9 and Figure 10, a simplified geometric closure framework was developed based on a two-dimensional cross-sectional representation of the deflected membrane. Although the actual membrane deformation is three-dimensional, the framework approximates the membrane profile in cross-section as a symmetric circular arc, traced by the dashed circle in Figure 11. The effective width of the deformable membrane region — the initial undeformed lateral extent that is free to deflect into the valve-seat cavity — forms the base, and therefore the chord length C, of this arc. Importantly, this membrane width is not necessarily identical to either the flow-channel width or the control-channel width but is instead determined by the geometry of the deformable cavity and valve-seat region beneath the membrane. The chord C in turn defines the radius R and sagitta s of the circular-arc approximation. These geometric relationships are packaged into an interactive, browser-based design tool, provided in the ESI, whose cross-sectional construction is reproduced in Figure 11.

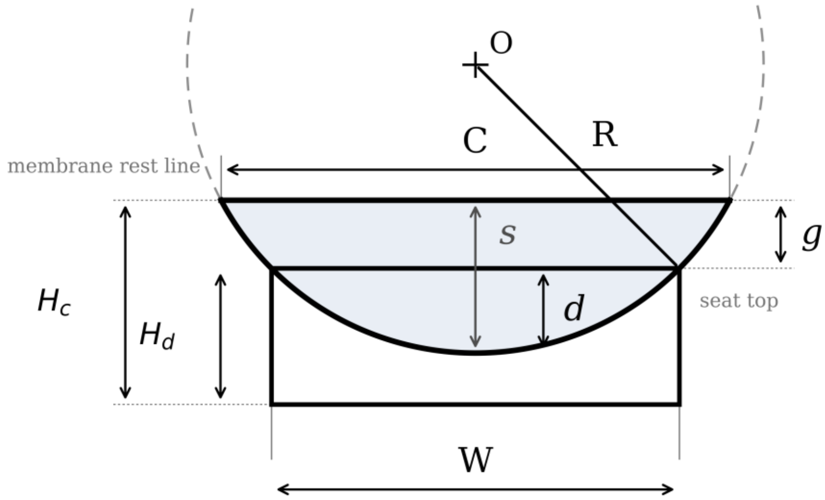

Figure 11 Geometric closure framework used to approximate membrane–seat conformity in stereolithographically printed membrane valves. *The membrane is modeled as a circular arc of chord length C, curvature radius R, and sagitta s. The flow-channel width W and the deformable membrane width C are two parallel chords of the same circle, separated vertically by the residual open-lumen height g. Derived quantities — the membrane deflection depth d below the seat top and the total channel height Hc (with valve-seat elevation Hd) — are shown for visualization of the geometric closure condition. Dimensions are illustrative and not to scale.*

A central simplification follows from this construction: the flow-channel width W and the deformable membrane width C are two parallel chords of the same circle, separated vertically by the residual open-lumen height g (see Figure 11). The valve is treated as sealed when the deflected membrane passes through the upper edges of the valve seat, so that the membrane conforms to a matched sealing geometry rather than merely touching a flat floor. Because this contact condition is imposed when the geometry is solved, every configuration the tool returns is, by construction, a sealing one; the deflection depth d by which the membrane continues below the seat top is a derived quantity, not a separate closure test. When the doormat height Hd is small — including $Hd = 0$, corresponding to a part-spherical seat recessed directly into the channel floor (see Figure 10-RIGHT) — the arc simply extends below the floor line, which reflects the recessed seat geometry and imposes no additional constraint. Moreover, because the membrane profile is represented as a circular arc, the same construction describes any sealing feature whose cross-section matches that arc: the segment of the circle below the seat-top chord equally represents a part-cylindrical channel floor (see Section 3.3.1) as it does a part-spherical recess (see Section 3.3.2). The framework therefore spans both sealing strategies without modification, underscoring its generality.

The only material-dependent input to the framework is a single empirical constant — the membrane deflection coefficient κ — that characterizes how far a given membrane deflects. For a membrane of fixed material, thickness, and actuation pressure, the sagitta grows with the deformable membrane width, and over a practical range this is well approximated by the linear relationship $s = \kappa * C$; κ is therefore the dimensionless sagitta-to-width ratio s/C. The coefficient κ is obtained experimentally, by measuring the sagitta of test membranes of several widths at a fixed control pressure — 30 psi for all measurements reported here — and fitting the slope of s versus C. Because the measured reach saturates once the membrane contacts the channel floor, the fit must be restricted to the pre-contact (free-deflection) regime: widths at which the membrane already reaches the floor are excluded, as are sub-onset widths at which no deflection is detected. In practice these sagitta values need not be measured separately — they are already contained in the membrane-reach data collected for functional characterization (see Figure 6), since membrane reach is defined as s/Hc × 100%. Because the sagitta is a vertical, layer-quantized dimension while the membrane width is a lateral, pixel-quantized one, both are converted to a common physical unit before forming the dimensionless ratio κ, following the quantized-unit convention introduced in Section 2.3. A worked illustration of this fit, together with the full unit-conversion discussion, is provided in Supplementary Materials. The complete set of quantities the user supplies and the tool returns is summarized in Table 1. Figure 11 serves as a visual key to this table: each quantity listed corresponds to a labeled dimension in the drawing.

Table 1 *Parameters of the geometric closure framework and interactive design tool. Input quantities are chosen or measured by the user; output quantities are returned by the tool.*

Inputs (set by the user)	**Outputs (returned by the tool)**
g — open-lumen height: residual flow gap under the fully deflected membrane ($g = s - d$)	*C* — required membrane width (width of the deformable membrane region)
κ — membrane deflection coefficient from the s–C fit (linear: s/C; power law: s/C^n)	*R* — radius of curvature of the deflected membrane
W — flow-channel width	*s* — sagitta: peak membrane deflection (rest line → arc bottom)
Hd — doormat (valve-seat) height; set 0 for a seat recessed into the channel floor	*d* — depth the membrane dips below the seat top ($d = s - g$)
n — power-law exponent (nonlinear model only; $n = 4/3$ ≈ large-deflection membrane)	*Hc* — total channel height ($Hc = Hd + g$)

Although the default implementation adopts the linear relationship s = κ*C for compactness and computational efficiency, the underlying geometric closure criterion is independent of this assumption. The tool therefore also provides a generalized nonlinear power-law relationship, s = κ*Cn, in which the exponent n is user-adjustable and defaults to n = 4/3; setting n = 1 recovers the linear model exactly. The default n = 4/3 is not empirical but follows from classical membrane mechanics: once the deflection substantially exceeds the membrane thickness, bending resistance becomes negligible and the applied pressure is carried almost entirely by in-plane stretching, for which the clamped-membrane solution gives a central deflection proportional to the cube root of the pressure and, at fixed pressure, to the 4/3 power of the width[63-65]. Both κ and n can be extracted from the same deflection measurements by fitting on logarithmic axes, where the slope gives n and the intercept gives ln κ. For the single-layer NanoClear membranes characterized in Section 3.2 this fit gives κ ≈ 0.075 at a channel height of 5 layers and κ ≈ 0.073 at 10 layers — a difference of about 3%, confirming that κ is a property of the membrane and print process rather than of the channel — with a fitted exponent $n \approx 1.26$. Because the measured exponent falls between strict proportionality ($n = 1$) and the stretching-dominated limit ($n = 4/3$), the linear default remains an adequate engineering approximation across the design range, with the mild supra-linearity in the direction theory predicts. The complete mathematical derivation of both the linear and nonlinear formulations, together with variable definitions and implementation details, is provided in the ESI (see Supplementary Note S1).

The tool itself allows the user to adjust the flow-channel width, membrane deflection coefficient, open-lumen height, and valve-seat elevation — either with sliders or by direct numerical entry — and immediately visualize the resulting membrane–seat geometry and the derived closure parameters in real time. The tool additionally includes a fitting utility that extracts κ (and, optionally, n) directly from measured deflection data while automatically excluding floor-contact-saturated points. Rather than functioning as a full mechanical simulation, it is intended as a geometry-guided design aid for identifying feasible sealing configurations and for understanding the geometric tradeoffs that govern membrane-valve closure in voxelized stereolithographic fabrication. The same closed-form solution is embedded in the parametric device generator provided with this work (see Data availability), which gives the Functionality Device of Figure 1B a second role beyond the membrane-reach measurement of Section 3.2. Printed without a sealing feature, it is the coupon from which κ is measured; once κ is known, the same file emits the seated geometries of Figure 10 — a raised doormat, a spherical recess, or both — with the seat radius and depth computed for each channel width from the two-chord construction of Figure 11 rather than chosen by hand, so that the recess spans the lumen by construction and rescales automatically when the channel width is swept. Because the device is open-faced, the resulting valve can then be actuated under the microscope and its closure confirmed directly in cross-section, which is how the seat profiles in the bottom row of Figure 12 were obtained. Design, fabrication and verification therefore close a loop within a single geometry: the coefficient measured on the plain coupon prescribes the seat, and the same coupon shows whether the prescribed seat in fact seals.

3.4. Functional Validation of the Selected Valve Architecture: Seat-Design Comparison, Operating Envelope, and Device-Level Demonstrations

3.4.1. Seat-Design Comparison Validates the Geometric Closure Framework

To test the central prediction of the closure framework, namely that sealing is governed by geometric conformity between the deflected membrane and the seat rather than by channel width per se, three seat geometries were fabricated at matched channel height and compared across the functional width range: (i) a plain rectangular (square) channel floor, serving as an unmodified baseline; (ii) a part-cylindrical (semi-rounded) channel floor (see Section 3.3.1), in which the membrane spans the flow channel directly so that the deformable membrane width is slaved to the channel width (“C” = “W”); and (iii) a doormat-mounted spherical-recess valve seat (see Section 3.3.2), in which the membrane width was prescribed independently of the channel width using the interactive design tool of Section 3.3.3.

The three seat geometries were compared by their leaked flow, expressed as a fraction of the open-valve flow, across channel widths from 60 to 120 printer pixels (see Figure 12). This range is the overlap of the printable and the functional windows established above: below about 60 px the membranes produce no measurable blocking action at the standard single-layer recipe, while the upper end stays inside the pre-sag-bounded functional limit of ~140 px identified in Section 3.2, with 120 px the widest width carried into full flow-device testing. Flow was driven at a constant 3 psi, and the valves were actuated at a control pressure of 30 psi.**Figure 12Figure 12** As expected, a plain rectangular (square) channel floor never sealed, leaking 90 to 100% at every width, because the flat floor cannot conform to the part-spherical inflated membrane. A part-cylindrical (semi-rounded) floor, over which the membrane spans the channel directly so that the deformable membrane width equals the channel width ("C" = "W"), improved with width: its leaked flow fell from about 100% at 60 px to roughly 50% at 120 px, as the wider and therefore more compliant membranes gained deflection capacity. This improvement with width may appear to run counter to the discretization argument of Section 3.3.1, in which a wider floor at fixed layer pitch is approximated by longer staircase steps and therefore larger leak gaps. The two effects act in opposite directions, and over this range the gain in membrane deflection capacity outweighs the coarser floor discretization; consistent with the discretization argument, however, the part-cylindrical floor never seals completely at any width. By contrast, the doormat with a spherical recess, whose membrane width "C" was prescribed independently of the channel width by the design tool of Section 3.3.3, sealed nearly completely across the entire range, leaking only 2 to 12% and thus varying far less with width than either of the other two geometries. This near-complete sealing, largely decoupled from channel width, is precisely the behavior predicted by the two-chord construction of Figure 11, in which decoupling "C" from "W" through the seat geometry removes the width dependence of closure.

This contrast constitutes a direct experimental confirmation of the framework. The doormat with spherical recess and tool-prescribed membrane width was therefore adopted for all subsequent characterization. In all adopted designs the open flow-channel height at the valve site is H = 5 layers (250 μm): the rectangular channel is five layers deep across its full width; the part-cylindrical channel reaches five layers at its deepest point, shallowing toward the edges; and in the doormat design the spherical recess is five layers deep at its lowest point.

Finally, a mixed-pitch ("multirange") printing strategy — 25 μm layers in the seat region for finer seat discretization, paired with a single 50 μm membrane layer — was explored as a route to further reduce discretization-induced leakage (see Section 3.3.1). In practice its complications outweighed the benefit: at 25 μm the default exposure schedule over-cured negative spaces; when the membrane itself was printed at the fine pitch — as two 25 μm layers rather than as one 50 μm layer — it was burst-prone and unprintable below 90 px width (in this variant the device was printed at 25 μm layers from the base up to just below the membrane, and at 50 μm layers from the membrane upward); and multirange prints introduced a new edge-burst failure localized at the boundary between the two layer-thickness ranges, suppressible only by relocating that interface at least two layers below the membrane plane and filleting the valve-chamber corners; full details are provided in Supplementary Note S2 (ESI). The complete print recipe used for all reported devices is provided in Supplementary Note S3 (ESI).

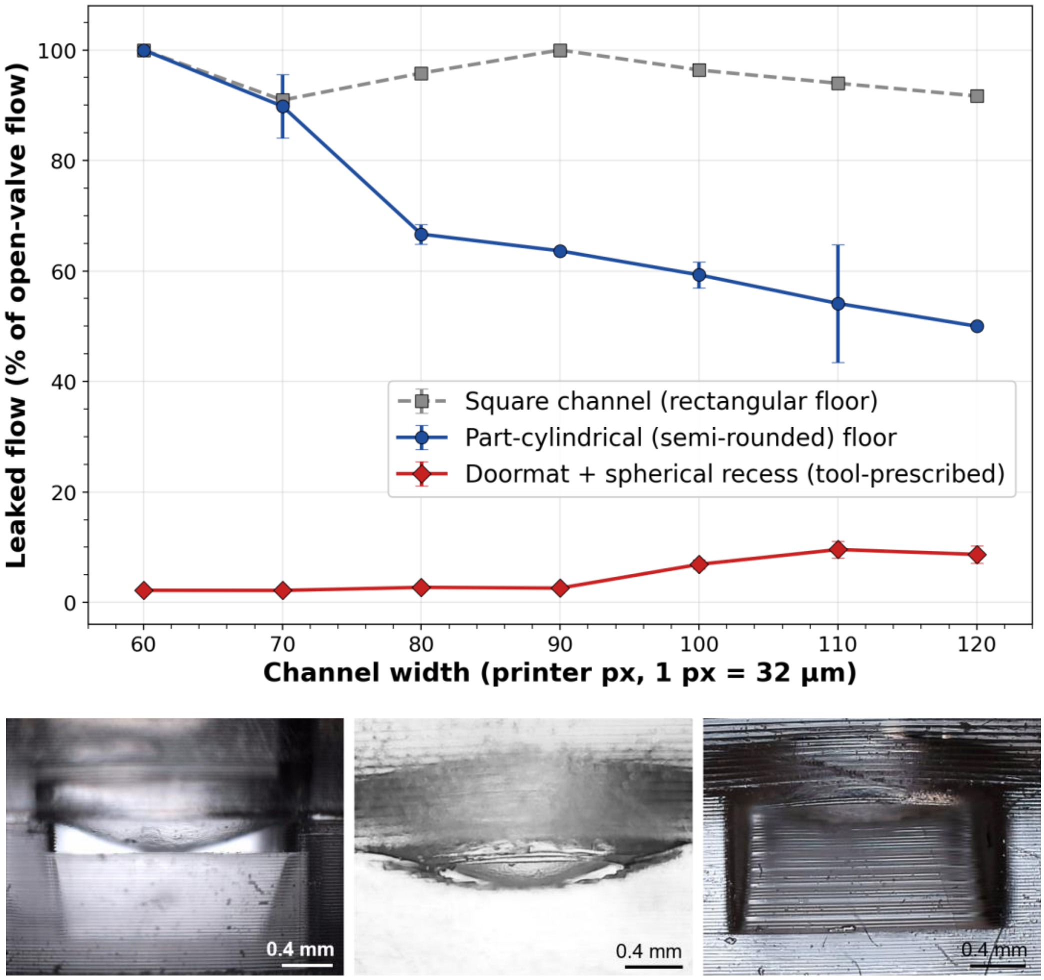

Figure 12 Leaked flow (percentage of open-valve flow) as a function of channel width for three sealing-feature geometries: a plain rectangular (square) channel floor, a part-cylindrical (semi-rounded) floor with a channel-spanning membrane ('C' = 'W'), and a doormat with a spherical recess whose membrane width 'C' is prescribed by the design tool. *Lower leaked flow indicates better sealing; symbols and error bars denote mean ± one standard error of the mean across three replicate devices. Leak flow was measured at a flow driving pressure of 3 psi and a control pressure of 30 psi. Only the doormat/spherical-recess design seals nearly completely, and it is the only one whose sealing is largely independent of channel width. Bottom row: representative cross-sectional micrographs of the three seat geometries at matched channel width, imaged in the open-faced Functionality Device (see Figure 1B) rather than in a complete valve so that the seat profile is visible in cross-section — (LEFT) plain rectangular (square) floor, (MIDDLE) part-cylindrical floor, (RIGHT) doormat with spherical recess. Scale bars (bottom row): 0.4 mm.*

3.4.2. Operating Envelope: Sealing Pressure, Burst Threshold, and Actuation Lifetime

Membranes that tolerated repeated quasi-static actuation in the open-faced Functionality Devices of Section 3.2 could nonetheless fail when operated against continuous flow, where the membrane must additionally overcome the hydrodynamic load. The operating envelope was therefore measured on complete flow devices — all of them built with the doormat/spherical-recess (spherical-cutout) seat geometry adopted in Section 3.4.1 — rather than on the open-faced Functionality Devices.

Flow-blocking efficiency, defined as the reduction in leak flow relative to the fully open valve, rose steeply with control pressure and reached complete blocking (zero measurable leak) at a width-dependent threshold pressure (Figure 13; mean ± standard error of the mean, n = 3 devices per condition)**Figure 13**. At 10 psi all widths leaked substantially (blocking efficiency below 20%), but by 20 psi every width exceeded 55% blocking. The narrowest valves sealed most readily: widths of 60 to 80 printer pixels achieved complete blocking by 30 psi, 90 to 100 px by 40 psi, and the widest 110 to 120 px valves required 50 psi, consistent with the larger membrane area that must be driven into conformal contact as width increases. Widths below 60 px produced no measurable blocking action at the standard membrane recipe and are omitted. All blocking measurements were performed at a constant 3 psi flow driving pressure.

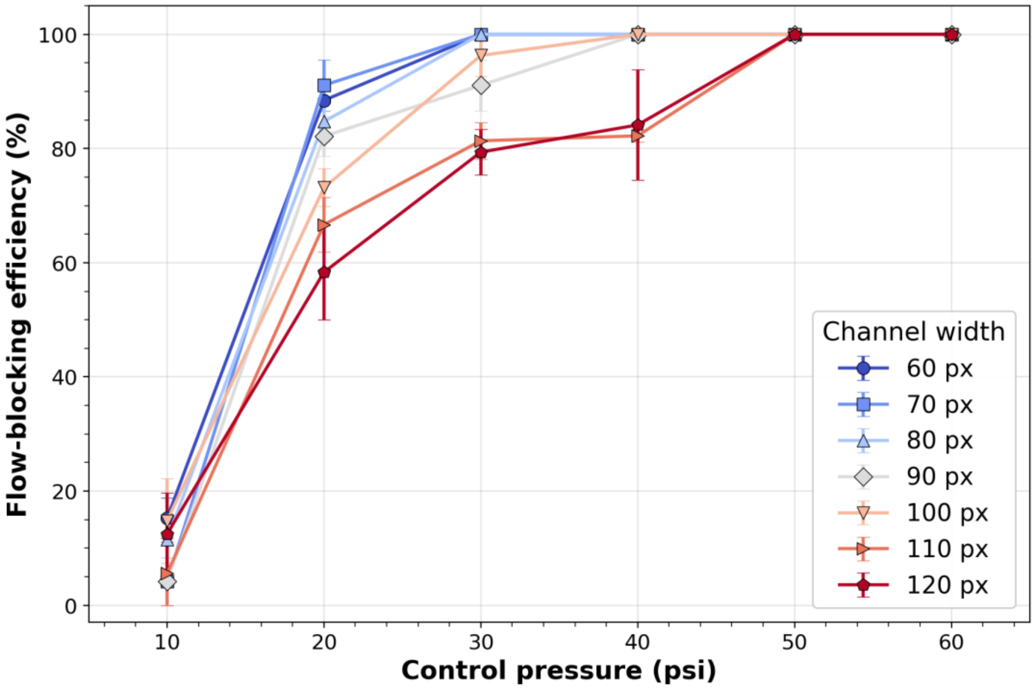

Figure 13 Flow-blocking efficiency of doormat/spherical-recess valves as a function of applied control pressure, for channel widths from 60 to 120 printer pixels (1 px = 32 µm). *Blocking efficiency is the percentage reduction in leak flow relative to the open valve; symbols and error bars denote mean plus/minus one standard error of the mean across three replicate devices. Complete blocking is reached at progressively higher control pressures as channel width increases. Flow driving pressure: 3 psi.*

Burst thresholds were mapped by stepping the control pressure from 10 to 60 psi in 10 psi increments (Figure 14A; three replicate devices per width). All channel widths from 60 to 110 printer pixels remained intact across the entire 10 to 60 psi range. Only the widest 120 px valves failed, bursting in all three replicates at 50 psi and above. This defines a safe control-pressure envelope of at least 40 psi for every width, and full 60 psi tolerance for widths up to 110 px, comparing favorably with the 50 psi fluid-side pressure tolerance reported for 3D-printed one-way valves[10], although that figure pertains to a different (one-way) valve configuration and was not accompanied by a test protocol, so the comparison is indicative rather than like-for-like. Notably, the 120 px valve requires 50 psi to seal completely (see Figure 13) **Figure 13**yet bursts at that same pressure, so the 110 px width is the widest that both seals fully and survives, and is the recommended upper bound for reliable operation. All burst tests were performed with the flow channel filled with dyed water (90% water, 10% food dye) so that the moment of membrane failure could be visualized; the ramp was applied against a static, fluid-filled flow channel with no imposed flow or fluid-side pressure.

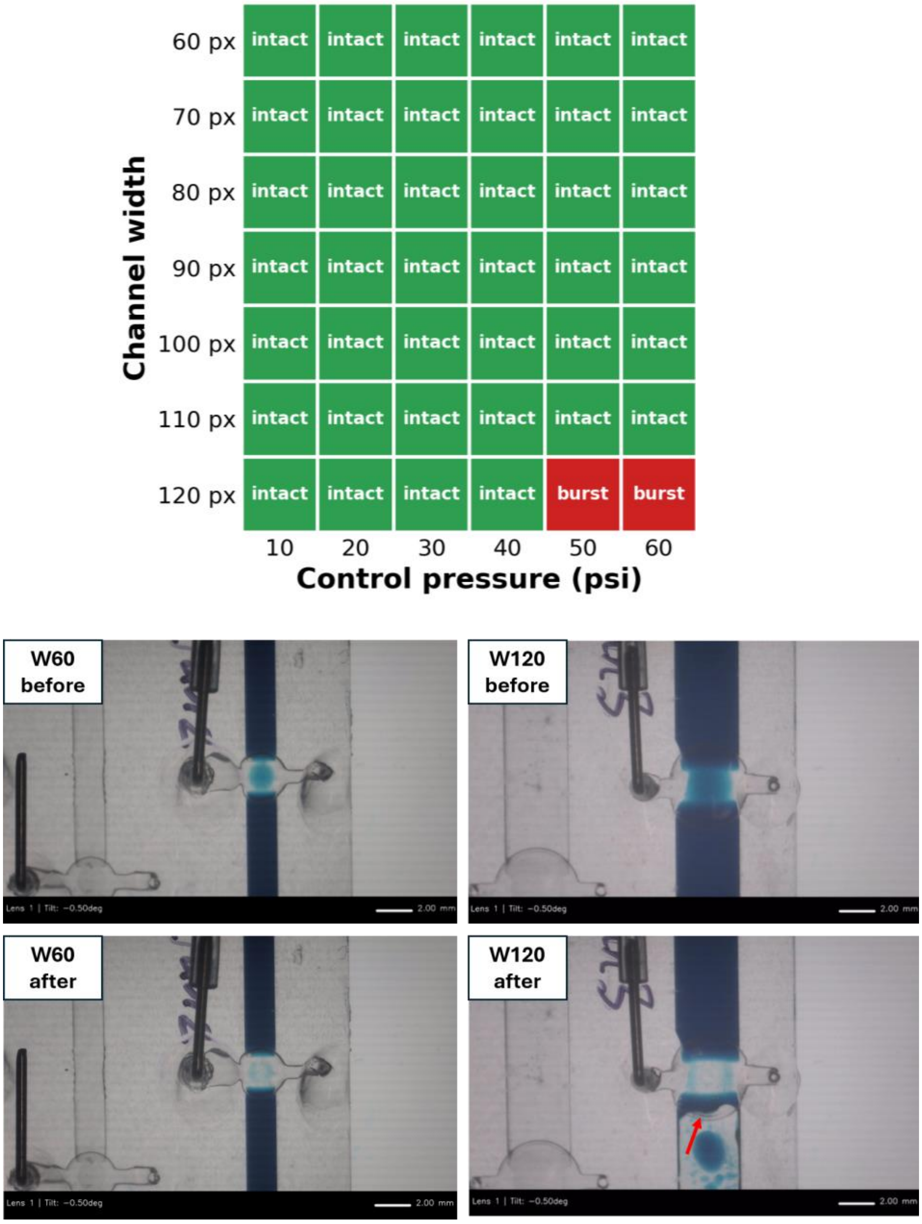

Figure 14 Burst-pressure envelope and million-cycle durability of the doormat/spherical-recess valves. *(A) Burst-test matrix for doormat/spherical-recess valves: green cells denote membranes that remained intact and red cells denote burst membranes, for channel widths of 60 to 120 printer pixels across control pressures of 10 to 60 psi (three replicate devices per cell; a cell is marked burst if any replicate failed). Only the 120 px valves burst, failing in all three replicates at both 50 and 60 psi. (B) Representative dye-filled valves before and after 1,000,000 actuation cycles: the 60 px device (left pair) is unchanged, whereas the 120 px device (right pair) shows dye penetrating beneath the membrane after cycling, indicating membrane tear. Scale bars: 2 mm.*

Durability was assessed over 1,000,000 open/close cycles (see Figure 14B)**Figure 14**. All widths up to and including 110 px completed the full million cycles without failure or measurable performance change; only the 120 px valves exhibited membrane tearing. This one-million-cycle lifetime matches the highest previously reported for a 3D-printed membrane valve (see Table 2)**Table 2**, which required a custom resin containing a thermal initiator together with a post-print thermal bake[5]; here the same lifetime was obtained with an unmodified commercial resin under default-class print settings.

Table 2 *Reported actuation lifetimes of 3D-printed membrane microvalves.*

Report	Printer / resin	Valve type	Demonstrated lifetime
Rogers et al. 2015 [47]	SLA, custom PEG-DA resin	membrane (doormat-style)	~800 cycles (membrane rupture)
Gong et al. 2016[5]	DLP-SLA, custom resin + thermal initiator/post-bake	membrane, high-density	52/54 valves to 10,000; one valve to 1,000,000 after thermal post-cure
Lee et al. 2018 [6]	SLA, PEG-DA-258	Quake-style	over 500,000 cycles (16 h at 10 Hz)
This work	DLP, commercial NanoClear (default-class settings)	doormat + spherical-recess seat, monolithic	1,000,000 cycles (all widths to 110 px intact; tear at 120 px)

3.4.3. Device-Level Demonstrations: Multi-Way Flow Routing and On-Chip Pumping

Two device-level demonstrations establish that the validated valve supports the canonical operations expected of printed microfluidic logic. First, a three-way flow-redirection device integrating three independently addressable valves demonstrated both state-retaining sequential addressing, in which channels one, two, and three are filled in sequence while previously filled channels hold their state, and single-channel addressing by a fill-flush-fill sequence (Figure 15; ESI Videos S7.1 and S7.2).**Figure** 15

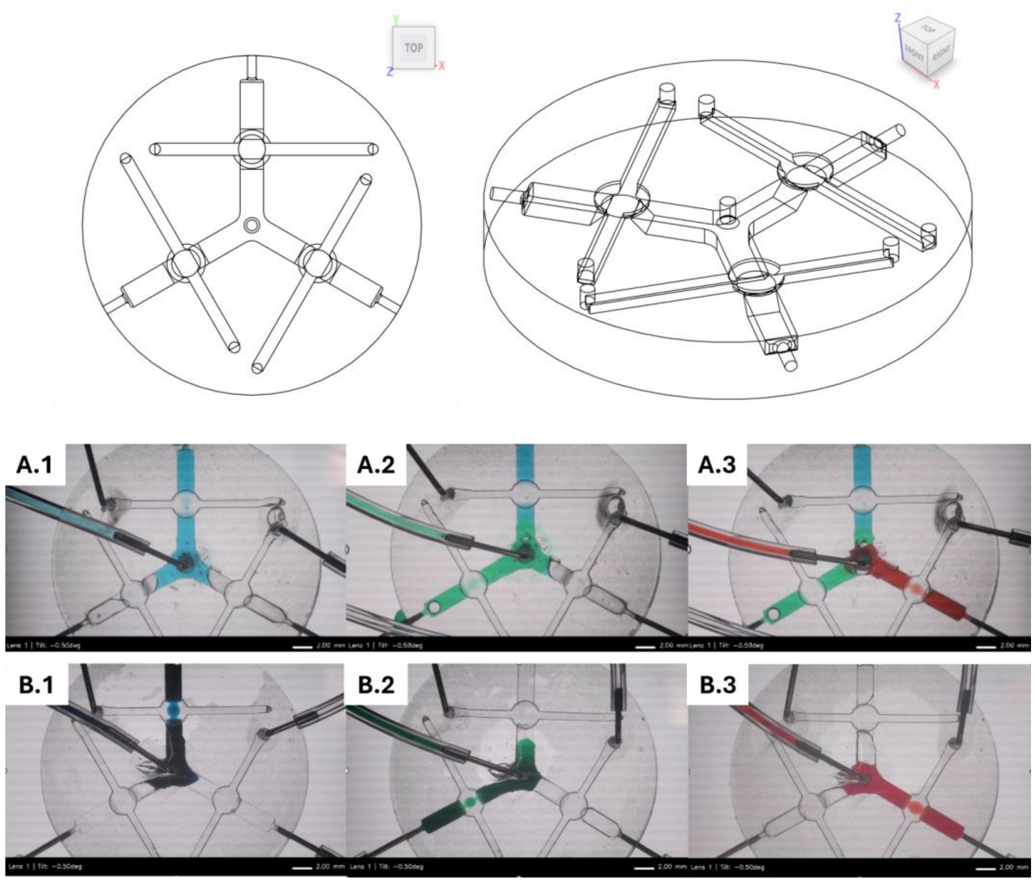

***Figure** 15 **Three-way flow-redirection device.** (TOP-left) Top-view CAD and (TOP-right) perspective view of the device, integrating three independently addressable valves. (A.1-A.3) State-retaining sequential addressing: dye is introduced from the top inlet into each of the three arms in the order blue, green, red, and previously filled arms retain their contents. (B.1-B.3) Single-channel addressing by a fill-flush-fill sequence: blue, flush, green, flush, red. Scale bars: 2 mm.*

Second, an on-chip pump was realized by actuating three valve chambers in the six-phase peristaltic sequence described in Section 2.8, drawing fluid from a reservoir and discharging to waste (Figure 16; ESI Video S8). At a valve actuation frequency of 5 Hz, the pump delivered a net flow rate of 20.6 ± 1.3 μL/min, corresponding to a displaced volume of 0.412 ± 0.026 μL per full six-phase cycle (cycle frequency 0.83 Hz; 0.069 ± 0.004 μL per phase). Because delivery requires each valve to complete its stroke within the 0.2 s phase interval, the measured pumping also bounds the valve open/close response time below 200 ms. For context, this places the device at the upper end of the range reported for 3D-printed pneumatic membrane pumps, and well above the original multilayer soft-lithography peristaltic pump: Gong et al. reported up to 40 μL/min using vacuum-assisted five-phase actuation at a 15 ms phase interval,[5] Lee et al. measured a maximum of about 6.5 μL/min at 20 Hz,[6] and the original PDMS Quake-style peristaltic pump delivered 2.35 nL/s (0.14 μL/min) at 75 Hz.[11] The present pump reaches comparable throughput by a different route, however: its displaced volume per cycle (0.412 μL) is five- to ten-fold larger than the tens of nanoliters per cycle reported for those printed pumps, while its cycle frequency (0.83 Hz) is more than an order of magnitude lower — a direct consequence of the large valve chambers (250 μm-tall channels a few millimeters wide) that the geometry-first framework identifies as printable in a commercial resin under default settings. Practically, 20 μL/min is ample for the perfusion and reagent-delivery duty cycles typical of integrated microfluidic assays, and the low actuation frequency is what makes the one-million-cycle lifetime reported above compatible with a realistic operating life. Maximum back-pressure was not measured, so the device is characterized here by free-delivery flow rate alone.**Figure 16**

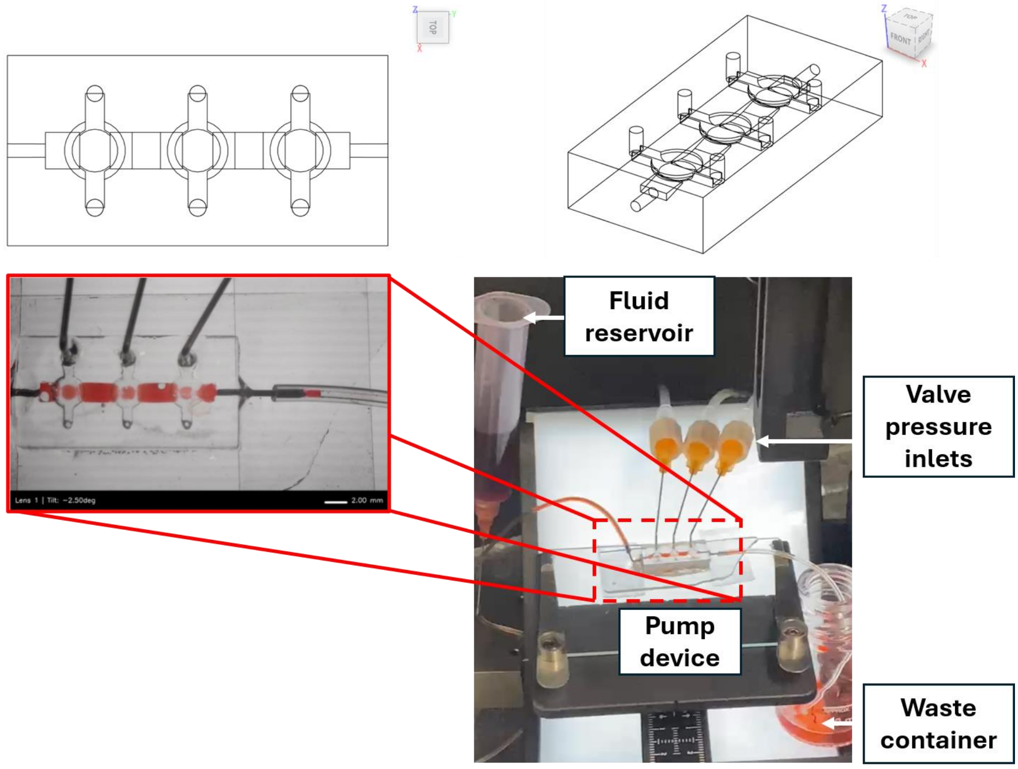

Figure 16 On-chip peristaltic pump. *(TOP-left) Top-view and (TOP-right) perspective CAD of the three-chamber pump device. (BOTTOM-left) Zoomed-in micrograph of the printed device. (BOTTOM-right) Experimental setup during six-phase actuation: the fluid reservoir and waste container are placed level with the pump device and connected by 1/32 in. ID × 1/16 in. OD tubing; the valve chambers are driven by solenoid valves via 1/16 in. ID × 1/8 in. OD tubing and 23G needles. Scale bar (zoomed micrograph): 2 mm.*

3.5. Generality of the Framework Across Valve Architectures and Materials

3.5.1. Across Valve Architectures

Because the printability and membrane-feasibility bounds established in Sections 3.1 and 3.2 are independent of valve topology, they apply to any membrane-based valve architecture. To demonstrate this we fabricated three canonical monolithic valve architectures — Quake, Plunger, and Squeeze valves — solely to validate geometric feasibility in NanoClear (see Figure 17). These valve types were selected because they span distinct modes of membrane deformation and channel interaction, providing a stringent test of the generality of the framework. Top- and side-view optical microscopy confirmed that suspended membranes, valve chambers, control channels, and sealing features printed cleanly and conformed to their intended geometries across all three architectures.

Critically, the three architectures do not merely share printable dimensions: each seals against a spherical seat designed with the web-based design tool provided in the ESI (see Section 3.3.3), its curvature fixed by the same membrane deflection coefficient κ, yet they realize this seat through three distinct embodiments that together map the breadth of the framework. The Quake valve uses a single doormat-mounted spherical recess beneath its ceiling membrane, following the seated-membrane approach previously demonstrated for 3D-printed Quake-style valves.[6] The Plunger valve seals a dome-shaped membrane against a matched part-spherical seat; plunger valves paired with shaped valve seats have been reported previously — for example, by Winkler et al.[48] Such shaped seats are best understood as geometric aids that compensate for the fixed process window of commercial printers and resins — where neither print resolution nor membrane compliance can be freely tuned — by using geometry to assist membrane flexure within the printable range. What distinguishes the present implementation is that the seat curvature is not chosen ad hoc but prescribed by the κ-based closure framework of Section 3.3.3. The Squeeze valve, by contrast, is an established architecture that the framework led us to redesign. Previously reported squeeze valves — realized in custom resins or on custom printers — pinch the lumen between two unshaped opposed membranes and carry no valve seat at all, a configuration that depends on membrane compliance which the commercial resin used here does not provide: the two opposed membranes meet only along their centerlines, so the lumen pinches shut at mid-span while the flanks on either side remain open and continue to pass flow — the same residual-leak mode seen in an unseated Quake valve over a plain rectangular floor. Matching each membrane with a spherical-cap seat cut to its deflected profile closes those flanks, so the pinch seals across the full lumen width. Guided by the geometric framework of Section 3.3.3 we therefore added a feature that, to our knowledge, has not been reported: because both the floor and the ceiling of the flow channel are flexible membranes, the redesigned valve carries two mirrored spherical-cap seats — one guiding each membrane — supported by the rigid channel side walls, which assume the structural role that the doormat plays in the stacked (Quake and Plunger) architectures. The closure framework therefore generalizes not only across printable geometries but across fundamentally different actuation modes (vertical membrane deflection in the Quake valve, axial displacement of a piston-like membrane in the Plunger valve, and simultaneous deflection of opposed floor and ceiling membranes in the Squeeze valve), each sealing against the same κ-prescribed spherical-arc geometry. The dual-seat Squeeze valve in particular serves as the capstone of this generality argument: it shows that a single empirical membrane deflection coefficient can be transferred not only to a new resin but to a previously unrealized valve topology. This breadth indicates that the geometric closure model of Section 3.3.3 captures a mode-independent sealing principle rather than a device-specific recipe.

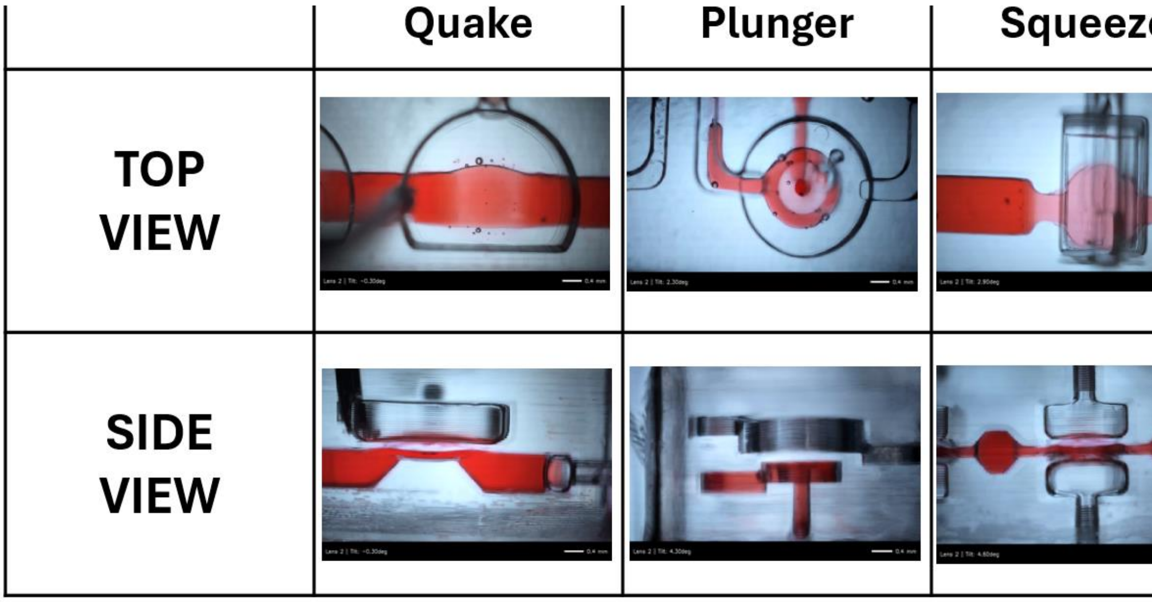

Figure 17 Geometric demonstration of Quake, Plunger, and Squeeze valve designs printed in NanoClear. *Top and side views show accurate formation of suspended membranes, chambers, and sealing features within*

the defined printability bounds. Red food dye on the flow-channel side provides visual clarity of the valve action. Scale bars: 0.4 mm.

No comparative functional characterization across valve architectures, including pressure thresholds, leak rates, or durability testing, was performed at this stage. The purpose of this demonstration is limited to confirming that the geometric constraints identified in Sections 3.1–3.4 are sufficient to support the fabrication of diverse valve topologies using a single, previously uncharacterized resin. The successful realization of these architectures provides validation that the proposed heuristic is not limited to a specific valve design but can be applied broadly to membrane-based microfluidic valves.

3.5.2. Across Resins (Second Commercial Photopolymer)

To evaluate whether the proposed geometry-first framework is specific to NanoClear or generalizable across materials, we applied the same constraint-propagation workflow to a second commercial photopolymer resin, Asiga Dental IBT. Dental IBT was selected because it differs substantially from NanoClear in formulation, intended application, and mechanical behavior, and is not marketed for microfluidic device fabrication.

Without modifying the framework or introducing resin-specific tuning rules, the geometric bounds identified through the same staged workflow — rigid-channel printability (Stage I), membrane functionality (Stage II), and sealing-feature prescription (Stage III) — were applied directly to IBT. Using these constraints, monolithic membrane-based valve geometries were fabricated successfully, exhibiting clean formation of suspended membranes, intact channel ceilings, and functional sealing features.

These results demonstrate that the proposed methodology does not rely on material-specific mechanical property data or prior valve recipes, and that geometric feasibility alone can guide valve design across chemically and mechanically distinct photopolymers. All three canonical valve architectures of Section 3.5.1 were likewise realized and actuated in IBT (Figure S5; Videos S1-S6, ESI). A more detailed quantitative characterization of IBT-based valves is beyond the scope of the present work.

3.6. Scope and Limitations of the Framework

Several limitations bound the scope of the present framework. Foremost, the closure model idealizes the deflected membrane as a spherical cap and prescribes a matching single-radius spherical seat. This idealization is exact only for a membrane with a circular boundary, which among the architectures realized here applies to the Plunger valve alone; the Quake and Squeeze membranes have rectangular footprints and therefore deflect into an only *approximately* spherical (pseudo-spherical) surface — in effect a part-ellipsoidal dome whose proportions depend on the membrane base aspect ratio. The spherical seat consequently matches the true membrane surface most closely near the membrane center and least well toward its corners and edges, where a residual gap can persist at full deflection. This mismatch is a plausible contributor to the small residual leakage that persists for the seated (doormat plus spherical-recess) design in Section 3.4 — a residual that, for that design alone, grows modestly with channel width, from about 2% at 60 px to about 12% at 120 px, consistent with those valves also requiring the highest control pressures to seal completely (see Figure 13). The two unseated floor geometries behave oppositely, their leakage falling with width for the reasons given in Section 3.4.1, but neither approaches complete sealing at any width. Extending the seat from a sphere to a membrane-shape-matched surface — for example a part-ellipsoidal recess parameterized by the same membrane deflection coefficient κ — would be a natural refinement, at the cost of added design and print complexity.

Two further limitations should be noted. First, the membrane deflection coefficient κ is an empirical, resin- and process-specific quantity: it folds together the resin modulus, the cured membrane thickness, and the exposure conditions, and the post-processing protocol (solvent washing and post-curing can alter the stiffness of the cured membrane), and must be re-measured whenever any of these change. In principle, a different printer reproducing the same resin, layer pitch, and exposure schedule — and therefore the same cured membrane thickness and stiffness — should yield the same κ; in practice light-engine intensity, pixel size, and optical uniformity differ between machines, so κ should be re-fitted rather than assumed to transfer. The cost of doing so is low, since the fit requires only the reach data from a single Functionality Device coupon. Second, the feasibility bounds are established under a worst-case printability criterion — the widest channels, spanned by free-edged roofs, and closure was characterized only up to the width at which the roof pre-sags beyond the open-lumen baseline (approximately 150 printer pixels here, which bounds the demonstrated functional range at ~140 px); behavior beyond that bound lies outside the validated envelope. These constraints delimit where the framework applies rather than undermining it: within the stated bounds, a single geometric coefficient continues to predict sealing across resins and valve architectures. One boundary runs the other way. Nothing in the closure model refers to how the geometry is produced: it operates on the deflected membrane cross-section, and its single material input, κ, is measured rather than derived. The model therefore applies to any fabrication route in which a compliant membrane of prescribed width can be formed and its sagitta measured, whereas the printability stages of Sections 3.1 – 3.2, the layer-discretized seat treatment of Section 3.3.1, and the pixel- and layer-quantized input mode of the design tool are specific to vat photopolymerization. Only printed devices are demonstrated here, so this wider applicability is a property of the model rather than a result of the present study.

4. Conclusions

This work presents a systematic, geometry-first framework for fabricating membrane-based microfluidic valves using light-based 3D printing when working with newly adopted photopolymer resins that lack relevant mechanical property data. Rather than relying on black-box, intuition-driven trial-and-error device iteration, the proposed approach incrementally constrains the design space through a sequence of printability and geometric feasibility tests, each tied to a physically motivated characteristic length scale within the system, and packages the final sealing-geometry step in an interactive browser-based design tool provided in the ESI. Commercial resins are the deliberate target of this approach: they are inexpensive, available off the shelf with vendor-validated print settings, and require no formulation chemistry, which is what makes valve fabrication accessible to laboratories that cannot mix and qualify their own photopolymers — but it is also why their membrane-relevant properties are undocumented, and therefore why a geometry-first route is needed.

Using the commercial resin FunToDo NanoClear as an illustrative case, we demonstrate how channel-ceiling printability, membrane thickness–width limits, membrane reach, and sealing-feature geometry can be evaluated independently to define a reproducible and bounded design space for valve fabrication. The framework isolates geometric feasibility from functional performance, allowing users to determine whether a given resin can support compliant membrane structures before undertaking pressure, durability, or flow characterization. This split is embodied in two complementary test devices: the passive Printability Device provides a quick, low-cost, yet predictive estimate of the feasible geometry, while the Functionality Device delivers the definitive assessment of whether an actuated valve will in fact work. When that characterization was subsequently performed for the selected NanoClear geometry (see Section 3.4), the valves blocked flow completely at 30 to 50 psi control pressure depending on channel width, tolerated control pressures of up to 60 psi for widths up to 110 printer pixels before the widest valves burst, survived one million actuation cycles at all but the widest tested channel width (matching the best durability previously reported, which there required a custom thermally post-cured resin), and supported device-level flow routing and on-chip pumping.

By expressing valve design as a series of convergent geometric decisions—rather than as an open-ended optimization problem—this methodology lowers the barrier to implementing active components in 3D-printed microfluidic devices and reduces dependence on proprietary materials or undocumented resin behavior. Although developed here with NanoClear and reaffirmed with Dental IBT — a dental material not previously used for microfluidics — the framework is material-agnostic and directly applicable to other commercial photopolymers, providing a practical pathway for evaluating valve feasibility in emerging 3D-printed microfluidic workflows. The closure model at the core of the framework is agnostic to fabrication method as well as to material: it acts only on the deflected membrane cross-section and requires only a measured κ, so it carries over to any process in which a compliant membrane of prescribed width can be formed and its deflection measured, even though only printed devices are demonstrated here. That the framework is generative as well as descriptive is shown by the valve it prompted: a previously unreported dual-seat squeeze design in which two mirrored spherical-cap seats, prescribed by the same membrane deflection coefficient κ, guide opposed floor and ceiling membranes to closure. Future work will focus on complementing the present geometric bounds with a systematic framework for selecting printer process parameters — exposure schedule, layer pitch, and post-processing — extending the same feasibility-first philosophy from geometry to process.

Author contributions

Roman Voronov: Conceptualization, Supervision, Project administration, Funding acquisition, Software (MATLAB image-analysis and OpenSCAD design code), Formal analysis, Writing – original draft, Writing – review & editing. Huu Anh Minh Nguyen: Investigation (microfluidic experiments), Data curation, Formal analysis, Writing – original draft (including literature review), Writing – review & editing. Nhu Doan Quynh Nguyen: Investigation (microfluidic experiments), Writing – original draft (including literature review). Quynh Ai Vuong: Investigation (microfluidic experiments), Writing – original draft (including literature review). Mark Volosov: Resources (custom actuation/control hardware), Software. Dae Jung Martins Cruz: Resources (custom actuation/control hardware), Software. Bernardino Almanzar: Resources (custom actuation/control hardware), Software. Abigail Goz: Software (OpenSCAD device generation). Maanit Khanna: Software (OpenSCAD device generation). Rishabh Jitender: Software (OpenSCAD device generation). Sergei Chapek: Conceptualization (3D device design). Aidan Kinney: Investigation (microfluidic experiments).

Acknowledgements

This work was supported by the National Institutes of Health (NIH) grant number 1R15GM145610-01, the National Science Foundation (NSF) Award Number 2141029 and the New Jersey Health

Foundation (Foundation for Health Advancement, Inc.) Innovation Grant Award Number IFHA 10-22.

Declaration of generative AI and AI-assisted technologies in the writing process

During the preparation of this work the authors used OpenAI ChatGPT, Google Gemini Pro, and Anthropic Claude (Opus and Fable) to check grammar; to implement and optimize the MATLAB image-analysis and data-processing code described in Section 2.7; to implement the interactive design tool provided in the ESI; and to assist in developing the mathematical formulation of the geometric closure framework presented in Section 3.3.3. The underlying concepts — the geometry-first framework itself, the image-analysis approach and processing pipeline, and the closure model on which the design tool is based — were conceived and specified by the authors; the AI tools were used to express them in code and in mathematical form, and to tune parameters, under author direction and against author-supplied test cases. The authors reviewed and edited all resulting content, verified the derivations and numerical results, and take full responsibility for the content of the publication.

Conflicts of interest

There are no conflicts to declare.

Data availability

The OpenSCAD source files used to parametrically generate the Printability and Functionality Devices are archived at Zenodo, DOI: 10.5281/zenodo.21984154, and developed at https://github.com/iomega15/3d-printed-microfluidic-valve-testing-device-generators. The interactive design tool is provided in the ESI, is archived at Zenodo, DOI: 10.5281/zenodo.21984175, and is developed at https://github.com/iomega15/microfluidic-valve-design-calculator, with a browser-hosted copy at https://iomega15.github.io/microfluidic-valve-design-calculator. Both DOIs are version-independent and resolve to the most recent release of the corresponding software. The eight supplementary videos (ESI Videos S1–S8) are archived at Zenodo, DOI: 10.5281/zenodo.22051901, which is likewise version-independent. The image-analysis code and the underlying measurement data are available from the corresponding author on reasonable request.

References

(1) Gong, H.; Bickham, B. P.; Woolley, A. T.; Nordin, G. P. Custom 3D printer and resin for 18 μm× 20 μm microfluidic flow channels. *Lab on a Chip* **2017**, *17* (17), 2899-2909.
(2) Bhattacharjee, N.; Urrios, A.; Kang, S.; Folch, A. The upcoming 3D-printing revolution in microfluidics. *Lab on a Chip* **2016**, *16* (10), 1720-1742.
(3) Au, A. K.; Huynh, W.; Horowitz, L. F.; Folch, A. 3D-printed microfluidics. *Angewandte Chemie International Edition* **2016**, *55* (12), 3862-3881.
(4) Weisgrab, G.; Ovsianikov, A.; Costa, P. F. Functional 3D printing for microfluidic chips. *Advanced Materials Technologies* **2019**, *4* (10), 1900275.
(5) Gong, H.; Woolley, A. T.; Nordin, G. P. High density 3D printed microfluidic valves, pumps, and multiplexers. *Lab on a Chip* **2016**, *16* (13), 2450-2458. DOI: 10.1039/C6LC00565A.
(6) Lee, Y.-S.; Bhattacharjee, N.; Folch, A. 3D-printed Quake-style microvalves and micropumps. *Lab on a Chip* **2018**, *18* (8), 1207-1214.

(7) Beauchamp, M. J.; Nordin, G. P.; Woolley, A. T. Moving from millifluidic to truly microfluidic sub-100-μm cross-section 3D printed devices. *Analytical and bioanalytical chemistry* **2017**, *409* (18), 4311-4319.
(8) Oskui, S. M.; Diamante, G.; Liao, C.; Shi, W.; Gan, J.; Schlenk, D.; Grover, W. H. Assessing and reducing the toxicity of 3D-printed parts. *Environmental Science & Technology Letters* **2016**, *3* (1), 1-6.
(9) Carve, M.; Wlodkowic, D. 3D-printed chips: Compatibility of additive manufacturing photopolymeric substrata with biological applications. *Micromachines* **2018**, *9* (2), 91.
(10) Hinnen, H.; Viglione, M.; Munro, T. R.; Woolley, A. T.; Nordin, G. P. 3D-printed microfluidic one-way valves and pumps. *Micromachines* **2023**, *14* (7), 1286.
(11) Unger, M. A.; Chou, H.-P.; Thorsen, T.; Scherer, A.; Quake, S. R. Monolithic microfabricated valves and pumps by multilayer soft lithography. *science* **2000**, *288* (5463), 113-116.
(12) Weerappuli, P.; Kojima, T.; Takayama, S.; Basu, A. Novel monolithic “Slightly-Open doormat”(SOD) valve enables efficient fabrication of highly-scalable microfluidic gas-on-gas multiplexer. *Sensors and Actuators B: Chemical* **2019**, *297*, 126776.
(13) Samuel, R.; Thacker, C. M.; Maricq, A. V.; Gale, B. K. Simple and cost-effective fabrication of microvalve arrays in PDMS using laser cut molds with application to C. elegans manipulation in microfluidics. *Journal of Micromechanics and Microengineering* **2014**, *24* (10), 105007.
(14) Paul, B. K.; Abhinkar, B. S.; Lee, S. High pressure hermetic compression seals for embedding elastomeric membrane microvalves in polymer microfluidic devices. *Precision engineering* **2011**, *35* (2), 348-354.
(15) Li, N.; Hsu, C. H.; Folch, A. Parallel mixing of photolithographically defined nanoliter volumes using elastomeric microvalve arrays. *Electrophoresis* **2005**, *26* (19), 3758-3764.
(16) Mosadegh, B.; Kuo, C.-H.; Tung, Y.-C.; Torisawa, Y.-s.; Bersano-Begey, T.; Tavana, H.; Takayama, S. Integrated elastomeric components for autonomous regulation of sequential and oscillatory flow switching in microfluidic devices. *Nature physics* **2010**, *6* (6), 433-437.
(17) Gleichweit, E.; Baumgartner, C.; Diethardt, R.; Murer, A.; Sallegger, W.; Werkl, D.; Koestler, S. UV/Ozone Surface Treatment for Bonding of Elastomeric COC-Based Microfluidic Devices. In *Proceedings*, 2018; Vol. 2, p 943. DOI: 10.3390/proceedings2130943.
(18) Hosokawa, K.; Maeda, R. A pneumatically-actuated three-way microvalve fabricated with polydimethylsiloxane using the membrane transfer technique. *Journal of micromechanics and microengineering* **2000**, *10* (3), 415. DOI: 10.1088/0960-1317/10/3/317.
(19) Warr, C.; Valdoz, J. C.; Bickham, B. P.; Knight, C. J.; Franks, N. A.; Chartrand, N.; Van Ry, P. M.; Christensen, K. A.; Nordin, G. P.; Cook, A. D. Biocompatible PEGDA resin for 3D printing. *ACS applied bio materials* **2020**, *3* (4), 2239-2244.
(20) Ahmadianyazdi, A.; Miller, I. J.; Folch, A. Tunable resins with PDMS-like elastic modulus for stereolithographic 3D-printing of multimaterial microfluidic actuators. *Lab on a Chip* **2023**, *23* (18), 4019-4032.
(21) Tong, A.; Voronov, R. A minireview of microfluidic scaffold materials in tissue engineering. *Frontiers in Molecular Biosciences* **2022**, *8*, 783268.
(22) Lima, R. A. The Impact of Polydimethylsiloxane (PDMS) in Engineering: Recent Advances and Applications. *Fluids* **2025**, *10* (2), 41.
(23) Toepke, M. W.; Beebe, D. J. PDMS absorption of small molecules and consequences in microfluidic applications. *Lab on a Chip* **2006**, *6* (12), 1484-1486.

(24) Berthier, E.; Young, E. W.; Beebe, D. Engineers are from PDMS-land, Biologists are from Polystyrenia. *Lab on a Chip* **2012**, *12* (7), 1224-1237.

(25) Kuncová-Kallio, J.; Kallio, P. J. PDMS and its suitability for analytical microfluidic devices. In *2006 international conference of the IEEE engineering in medicine and biology society*, 2006; IEEE: pp 2486-2489.

(26) Halldorsson, S.; Lucumi, E.; Gómez-Sjöberg, R.; Fleming, R. M. Advantages and challenges of microfluidic cell culture in polydimethylsiloxane devices. *Biosensors and Bioelectronics* **2015**, *63*, 218-231.

(27) Sia, S. K.; Whitesides, G. M. Microfluidic devices fabricated in poly (dimethylsiloxane) for biological studies. *Electrophoresis* **2003**, *24* (21), 3563-3576.

(28) Wang, Y.; Chen, S.; Sun, H.; Li, W.; Hu, C.; Ren, K. Recent progresses in microfabricating perfluorinated polymers (Teflons) and the associated new applications in microfluidics. *Microphysiological Systems* **2018**, *2*.

(29) Ong, L. J. Y.; Kasetsirikul, S.; Milton, L. A.; Nie, X.; Eiken, A. W.; Chirnside, J.; Young, L. M. G.; Nordin, G. P.; Toh, Y. C. 3D-Printed Unibody Microfluidic Devices for Organ-on-Chip Applications. *Advanced Materials Technologies* **2025**, *10* (22), e01056.

(30) Asiga. *Open Material Library*. https://www.asiga.com/open-material-library/ (accessed 2026 3/10/2026).

(31) Karotkiyan, R. V.; Sadyrin, E. V.; Nikolaev, A. L.; Chapek, S. V.; Vasiliev, A. S. Finite Element Modeling of Uniaxial Compression of Scaffolds. In *Dynamics of Discrete and Continuum Structures and Media*, Springer, 2025; pp 377-386.

(32) Sadyrin, E. V.; Karotkiyan, R. V.; Nikolaev, A. L.; Chapek, S. V.; Lapina, P. A.; Wang, Y.-C. In Situ Mechanical Testing and Microtomography of 3D-Printed Hard Tissue Scaffolds for Bioengineering Applications. In *Dynamics of Discrete and Continuum Structures and Media*, Springer, 2025; pp 599-616.

(33) Eid, M. E.; Gorbunov, D. N.; Shapovalov, V. V.; Nenasheva, M. V.; Protsenko, B. O.; Khramov, E.; Bulgakov, A. N.; Abrosimov, S. V.; Chapek, S. V.; Guda, A. A. In Situ XAS Diagnostics of Reductive Hydroformylation Reaction in Segmented Flow Under Elevated Pressure and Temperature. *Industrial & Engineering Chemistry Research* **2024**, *63* (35), 15397-15403.

(34) Ermakov, A. V.; Chapek, S. V.; Lengert, E. V.; Konarev, P. V.; Volkov, V. V.; Artemov, V. V.; Soldatov, M. A.; Trushina, D. B. Microfluidically assisted synthesis of calcium carbonate submicron particles with improved loading properties. *Micromachines* **2023**, *15* (1), 16.

(35) Marchenkova, M. A.; Chapek, S. V.; Konarev, P. V.; Ilina, K. B.; Peters, G. S.; Pisarevsky, Y. V.; Shishkov, V. A.; Soldatov, A. V.; Kovalchuk, M. V. 3D Printed Microfluidic Cell for SAXS Time-Resolved Measurements of the Structure of Protein Crystallization Solutions. *Crystals* **2023**, *13* (6), 938.

(36) Sadyrin, E. V.; Nikolaev, A. L.; Chapek, S. V.; Nazarenko, D. V.; Aizikovich, S. M.; Wang, Y.-C. Manufacturing quality evaluation of photopolymer resin 3d-printed scaffolds using microtomography. In *Sixty Shades of Generalized Continua: Dedicated to the 60th Birthday of Prof. Victor A. Eremeyev*, Springer, 2023; pp 619-630.

(37) FunToDo. *Nano Clear Resin (Clear) 1kg*. n.d. https://funtodo.eu/shop/nano-clear/nano-clear/ (accessed 2025 12/15).

(38) Asiga. *DentalBT Safety Data Sheet (SDS) and an Instructions for Use (IFU)*. https://www.asiga.com/materials-dental/ (accessed 2026 02/04).

(39) Thorsen, T.; Maerkl, S. J.; Quake, S. R. Microfluidic large-scale integration. *Science* **2002**, *298* (5593), 580-584.
(40) Marcus, J. S.; Anderson, W. F.; Quake, S. R. Microfluidic single-cell mRNA isolation and analysis. *Analytical chemistry* **2006**, *78* (9), 3084-3089.
(41) Mohan, R.; Schudel, B. R.; Desai, A. V.; Yearsley, J. D.; Apblett, C. A.; Kenis, P. J. Design considerations for elastomeric normally closed microfluidic valves. *Sensors and Actuators B: Chemical* **2011**, *160* (1), 1216-1223.
(42) Desai, A. V.; Tice, J. D.; Apblett, C. A.; Kenis, P. J. Design considerations for electrostatic microvalves with applications in poly (dimethylsiloxane)-based microfluidics. *Lab on a Chip* **2012**, *12* (6), 1078-1088.
(43) Hulme, S. E.; Shevkoplyas, S. S.; Whitesides, G. M. Incorporation of prefabricated screw, pneumatic, and solenoid valves into microfluidic devices. *Lab on a Chip* **2009**, *9* (1), 79-86.
(44) Weibel, D. B.; Kruithof, M.; Potenta, S.; Sia, S. K.; Lee, A.; Whitesides, G. M. Torque-actuated valves for microfluidics. *Analytical chemistry* **2005**, *77* (15), 4726-4733.
(45) Briones, J.; Espulgar, W.; Koyama, S.; Takamatsu, H.; Tamiya, E.; Saito, M. A design and optimization of a high throughput valve based microfluidic device for single cell compartmentalization and analysis. *Scientific reports* **2021**, *11* (1), 12995.
(46) Supakar, T.; Space, D.; Mejia, S.; Tan, R. Y.; Alston, J. R.; Josephs, E. A. Programmed Internal Reconfigurations in a 3D-Printed Mechanical Metamaterial Enable Fluidic Control for a Vertically Stacked Valve Array. *Advanced functional materials* **2024**, *34* (32), 2315419.
(47) Rogers, C. I.; Qaderi, K.; Woolley, A. T.; Nordin, G. P. 3D printed microfluidic devices with integrated valves. *Biomicrofluidics* **2015**, *9* (1).
(48) Winkler, S.; Menke, J.; Meyer, K. V.; Kortmann, C.; Bahnemann, J. Automation of cell culture assays using a 3D-printed servomotor-controlled microfluidic valve system. *Lab on a Chip* **2022**, *22* (23), 4656-4665.
(49) Grover, W. H.; Skelley, A. M.; Liu, C. N.; Lagally, E. T.; Mathies, R. A. Monolithic membrane valves and diaphragm pumps for practical large-scale integration into glass microfluidic devices. *Sensors and Actuators B: Chemical* **2003**, *89* (3), 315-323.
(50) Childers, K.; Freed, I. M.; Hupert, M. L.; Shaw, B.; Larsen, N.; Herring, P.; Norton, J. H.; Shiri, F.; Vun, J.; August, K. J. Novel thermoplastic microvalves based on an elastomeric cyclic olefin copolymer. *Lab on a Chip* **2024**, *24* (18), 4422-4439.
(51) Cheng, C.; Nair, A. R.; Thakur, R.; Fridman, G. Normally closed plunger-membrane microvalve self-actuated electrically using a shape memory alloy wire. *Microfluidics and nanofluidics* **2018**, *22* (3), 29.
(52) Zhang, X.; Oseyemi, A. E. Microfluidic passive valve with ultra-low threshold pressure for high-throughput liquid delivery. *Micromachines* **2019**, *10* (12), 798.
(53) Sanchez Noriega, J. L.; Chartrand, N. A.; Valdoz, J. C.; Cribbs, C. G.; Jacobs, D. A.; Poulson, D.; Viglione, M. S.; Woolley, A. T.; Van Ry, P. M.; Christensen, K. A. Spatially and optically tailored 3D printing for highly miniaturized and integrated microfluidics. *Nature communications* **2021**, *12* (1), 5509.
(54) Sundararajan, N.; Kim, D.; Berlin, A. A. Microfluidic operations using deformable polymer membranes fabricated by single layer soft lithography. *Lab on a Chip* **2005**, *5* (3), 350-354.
(55) Lai, H.; Folch, A. Design and dynamic characterization of "single-stroke" peristaltic PDMS micropumps. *Lab on a Chip* **2011**, *11* (2), 336-342. DOI: 10.1039/c0lc00023j.

(56) Tracey, M. C.; Johnston, I. D.; Davis, J. B.; Tan, C. K. L. Dual independent displacement-amplified micropumps with a single actuator. *Journal of Micromechanics and Microengineering* **2006**, *16* (8), 1444-1452. DOI: 10.1088/0960-1317/16/8/002.
(57) Leong, K. M.; Sun, A. Y.; Quach, M. L.; Lin, C. H.; Craig, C. A.; Guo, F.; Robinson, T. R.; Chang, M. M.; Olanrewaju, A. O. Democratizing access to microfluidics: rapid prototyping of open microchannels with Low-Cost LCD 3D printers. *Acs Omega* **2024**, *9* (45), 45537-45544.
(58) Schindelin, J.; Arganda-Carreras, I.; Frise, E.; Kaynig, V.; Longair, M.; Pietzsch, T.; Preibisch, S.; Rueden, C.; Saalfeld, S.; Schmid, B. Fiji: an open-source platform for biological-image analysis. *Nature methods* **2012**, *9* (7), 676-682.
(59) Kirillov, A.; Mintun, E.; Ravi, N.; Mao, H.; Rolland, C.; Gustafson, L.; Xiao, T.; Whitehead, S.; Berg, A. C.; Lo, W.-Y. Segment anything. In *Proceedings of the IEEE/CVF international conference on computer vision*, 2023; pp 4015-4026.
(60) Liu, J.; Ma, J.; Kim, J.; Bae, J. Parameter Optimization for High-Resolution Microfluidic Channel Fabrication Using a Commercial Low-Cost MSLA Printer. *Micromachines* **2026**, *17* (2), 236.
(61) O'Neill, P. F.; Kent, N.; Brabazon, D. Mitigation and control of the overcuring effect in mask projection micro-stereolithography. In *AIP Conference Proceedings*, 2017; AIP Publishing LLC: Vol. 1896, p 200012.
(62) Luo, Z.; Zhang, H.; Chen, R.; Li, H.; Cheng, F.; Zhang, L.; Liu, J.; Kong, T.; Zhang, Y.; Wang, H. Digital light processing 3D printing for microfluidic chips with enhanced resolution via dosing-and zoning-controlled vat photopolymerization. *Microsystems & Nanoengineering* **2023**, *9* (1), 103.
(63) Timoshenko, S.; Woinowsky-Krieger, S. Theory of plates and shells. 2nd ed.; McGraw-Hill, 1959.
(64) Landau, L. D.; Lifshitz, E. M.; Kosevich, A. M.; Pitaevskii, L. P. *Theory of elasticity*; Butterworth-Heinemann, 1986.
(65) Vlassak, J. J.; Nix, W. D. A new bulge test technique for the determination of Young's modulus and Poisson's ratio of thin films. *Journal of Materials Research* **1992**, *7* (12), 3242-3249.